Laura Campo-Deaño[1]
Departamento de Engenharia Mecânica,
CEFT,
Faculdade de Engenharia,
Universidade do Porto,
Rua Dr. Roberto Frias,
Porto 4200-465, Portugal
e-mail: campo@fe.up.pt

Mónica S. N. Oliveira
James Weir Fluids Laboratory,
Mechanical and Aerospace Engineering,
University of Strathclyde,
Glasgow G1 1XJ, UK
e-mail: monica.oliveira@strath.ac.uk

Fernando T. Pinho
Departamento de Engenharia Mecânica,
CEFT,
Faculdade de Engenharia,
Universidade do Porto,
Rua Dr. Roberto Frias,
Porto 4200-465, Portugal
e-mail: fpinho@fe.up.pt

A Review of Computational Hemodynamics in Middle Cerebral Aneurysms and Rheological Models for Blood Flow

Cerebrovascular accidents are the third most common cause of death in developed countries. Over recent years, CFD simulations using medical image-based anatomical vascular geometries have been shown to have great potential as a tool for diagnostic and treatment of brain aneurysms, in particular to help advise on the best treatment options. This work aims to present a state of the art review of the different models used in CFD, focusing in particular on modeling blood as a viscoelastic non-Newtonian fluid in order to help understand the role of the complex rheological nature of blood upon the dynamics of middle cerebral aneurysms. Moreover, since the mechanical properties of the vessel walls also play an important role in the cardiovascular system, different models for the arterial structure are reviewed in order to couple CFD and computational solid dynamics to allow the study of the fluid–structure interaction (FSI).
[DOI: 10.1115/1.4028946]

1 Introduction

Cerebral aneurysms are one of the most common cerebrovascular accidents and are associated with a high rate of mortality and disability, constituting one-third of deaths worldwide [1]. The growth and rupture of aneurysms are not well understood. They depend, among other things, on the action of flow-induced mechanical stresses upon the vessel walls, which are essentially defined by the pressure and hemodynamic stresses [2,3]. The flow inside an aneurysm involves a strong rotation component and depends strongly on blood rheology and geometrical features [4,5] such as aneurysm shape, orientation, the ratio between the aneurysm and parent vessel dimensions and neck diameter. The small length-scales and the pulsatile character of blood flow emphasize the non-Newtonian flow characteristics [6], which can be responsible for differences of up to 40–50% relative to the corresponding Newtonian flow characteristics [7]. In contrast, the blood behavior in the heart and large blood vessels is usually assumed to be Newtonian. Even though this assumption is fair in many situations, in other cases it is far from accurate, in particular in the smaller blood vessels [8,9].

Blood exhibits non-Newtonian behavior due to its complex mixture of proteins and of suspended cellular elements in plasma, like platelets, leucocytes, and mainly red blood cells (RBCs) (also called erythrocytes) [10,11]. In fact, if blood is allowed to rest for several seconds, stacks of red cells (rouleaux) form and eventually create an interconnected network, thus increasing its resistance to deformation and imparting an elastic response to blood. Rouleaux are broken up by shear and strain, with their size and structure determined by an equilibrium between formation dynamics and flow induced destruction mechanisms. This disruption mechanism together with the alignment of RBCs result in a shear-thinning behavior with a relative decrease in blood viscosity as shear rate ($\dot{\gamma}$) is increased for an intermediate region of $\dot{\gamma}$ ($\dot{\gamma}$ is the second invariant of the deformation rate tensor (**D**), i.e., $\dot{\gamma} = \sqrt{2\mathbf{D} : \mathbf{D}}$ with $\mathbf{D} = (\nabla\mathbf{v} + (\nabla\mathbf{v})^{\mathrm{T}})/2)$, up to values around $100\,\mathrm{s}^{-1}$. This critical shear rate is associated with the alignment/misalignment of RBCs [10–14] and its exact value depends on various factors as described in Sec. 3. The viscoelasticity of whole blood is another important non-Newtonian characteristic which is evident in various experimental observations. It is usually quantified using the relaxation time which is a measure of the time taken by the internal fluid structures to relax internal stresses imposed by the flow [15]. The complex rheological behavior of whole blood has been studied for a long time, but continues to be investigated as new and more sensitive rheological techniques become available [16].

The most common dimensionless numbers that characterize these kinds of viscoelastic fluid flows are the Reynolds number (Re), defined as the ratio between inertial and viscous forces, $\mathrm{Re} = \rho V L / \eta$, and the Weissenberg number (Wi), which is the ratio between elastic and viscous forces, $\mathrm{Wi} = \lambda V / L$ [17]. V represents the average velocity, L the characteristic length-scale and ρ, λ, and η are the density, relaxation time, and viscosity of the fluid, respectively. Compared to the flow in large arteries, in the human microcirculatory system Re decreases while Wi increases leading to enhanced viscoelastic effects [18], which highlights the importance of treating blood flow as a non-Newtonian fluid and in particular, as a viscoelastic fluid.

The recent rapid growth in computing power has made the numerical simulation of blood flow a topic of research, but the success of this endeavor requires the correct characterization and

modeling of real human blood behavior [7,19–22] by means of adequate non-Newtonian rheological constitutive models. This is particularly important when investigating the flow in small vessels and those in diseased conditions where their small length scales emphasize the non-Newtonian nature of blood as discussed above.

CFD has been progressively used for modeling the flow in diseased arteries and has gained favor as a tool for understanding and predicting cardiovascular diseases [23]. This is because in vivo accurate measurements of the flow field in arteries are difficult to perform, they are usually very costly and only possible for arteries that allow an easy optical access. Since blood vessels are opaque to visible light, this may involve the use of short wavelength radiation to which the vessels are transparent, the use of ultrasound, or even the intrusion of a small transparent duct to allow optical access [24,25]. Measurements in complex real geometries, such as cerebral aneurysms, are therefore very limited, and numerical models of blood flow can offer a complementary platform for easy testing in real patient-specific geometries modified to address the prevention of specific diseases.

The aim of this article is to review investigations of computational hemodynamics with emphasis on CFD studies in middle cerebral aneurysms. The structure of this review is the following: in Sec. 2 the hemodynamic and environmental factors affecting the formation of aneurysms and their classification according to shape, size, and location are presented; Sec. 3 summarizes the main key information needed for modeling cerebral aneurysms including the mechanical properties of the vessel walls, the corresponding soft tissue model, and the rheological model for blood with the different parameter values used in the literature; in Sec. 4, the use of patient-specific models in CFD is discussed; Sec. 5 reviews computational hemodynamics studies for middle cerebral aneurysms; finally in Sec. 6, we summarize the main remarks and reflect on future directions.

2 Aneurysms

"The term aneurysm comes from the Greek word *ana* which means *across* and *eurus* which means *broad*" [26]. Nowadays, it is referred to as a weakness or dilation of a wall artery, and it can occur at any point within the cardiac and peripheral vasculature, but mainly in the abdominal and thoracic parts of the aorta and in the brain near arterial bifurcations in the Circle of Willis [26,27]. When an aneurysm ruptures, a hemorrhage takes place, usually leading to death or morbidity, especially in the case of cerebral aneurysms.

2.1 Types of Aneurysms. According to the location of the aneurysms, it is possible to distinguish between three types:

— *Aortic aneurysms*: These aneurysms occur in the aorta, which is the main artery that carries blood from the heart to the rest of the body. Aortic aneurysms can be subdivided into thoracic aortic aneurysms that occur in the part of the aorta traveling through the thorax (chest), and abdominal aortic aneurysms that occur in the part of the aorta passing through the abdomen.
— *Peripheral aneurysms*: These aneurysms affect arteries other than the aorta or Circle of Willis. For instance, they can occur in the popliteal artery, which runs down the back of the lower thigh and knee, in the neck, in the arm, or in the femoral artery in the groin.
— *Cerebral aneurysms*: The most common type of cerebral aneurysms (≈85% of all cases) is formed around the anterior part of the Circle of Willis. The vessels involved in this case are the internal carotid arteries and the branches that supply the anterior and middle sections of the brain.

2.2 Shape and Size of Aneurysms. The aneurysms are very variable in shape and size, so a classification according to these characteristics is also common. It is possible to distinguish
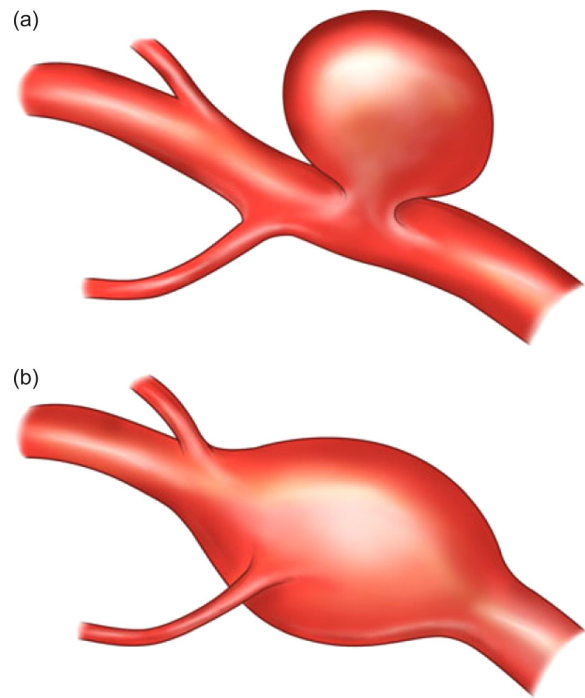

Fig. 1 Shapes of aneurysms: (*a*) saccular aneurysm and (*b*) fusiform aneurysm. (Reprinted with permission from Withers, K., et al. [28]. Copyright 2013 2.5 CC-BY-NC).

between essentially two types of aneurysm depending on their shape (Fig. 1):

— *Saccular* aneurysms: These are mostly cerebral aneurysms found along the Circle of Willis and more than 90% of the intracranial aneurysms are of this type [26]. They are localized deformations of the vessel into a berrylike or spherical shape, and they tend to form in curved arteries and near bifurcations [29].
— *Fusiform* aneurysms: These are most commonly found in the abdominal aorta or in the popliteal artery behind the knee [26]. They are abnormal dilations that involve the total circumference of the arterial wall. They are uncommon among cerebral aneurysms, with less than 1% frequency [30].

Since 90% of the middle cerebral aneurysms are of the saccular type, we will focus on this particular type of aneurysm hereafter.

Another important factor in the characterization of cerebral aneurysms is their size, since it is closely related with the risk of rupture [31]. A good understanding and identification of the geometry of real aneurysms is of great interest for the diagnostic and treatment of aneurysms. Parlea et al. [32] characterize the geometry of different kinds of saccular aneurysms based on their size and shape. According to their nomenclature (Fig. 2), the dimensions obtained by angiographic tracings are the neck width (N), the dome diameter (D), the dome height (H), and the dome semi-axis height (S). The angle, β, at which the dome tilts with respect to the parent vessel is also presented in Fig. 2. A second angle α gives the position of the aneurysms relative to the plane of the vessels at the bifurcation (the plane of the paper), but for simplicity we consider here only aneurysms in the plane of the vessels. For $D/H \ll 1$, the shape of the aneurysm is an ellipsoid, with the major axis in the vertical direction; for $D/H = 1$ it becomes a circle and for values $D/H \gg 1$ an ellipse is again observed, but now with the major axis in the horizontal direction. On the other hand, for $H/S \ll 2$, the aneurysm has a pear shape, for $H/S = 2$, it is a circle, and for $H/S \gg 2$ a beehive shape is found. Based on their extensive results of 87 simple-lobed aneurysms located in
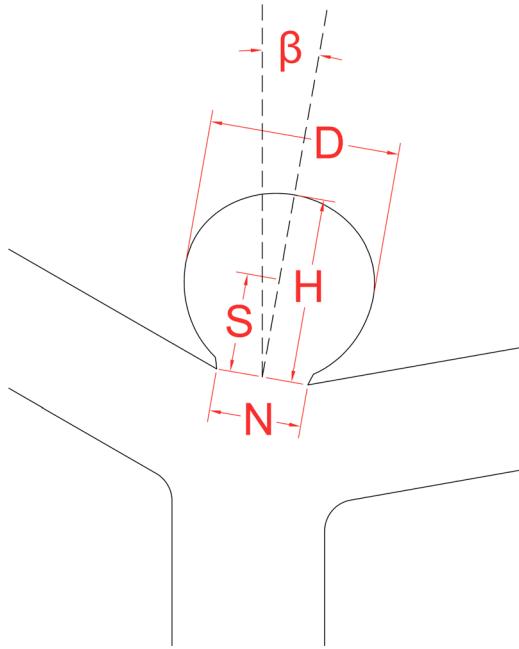
Fig. 2   Representation of the aneurysms dimensions

has been used quite successfully in this context. "It is used in curve theory to measure the extent to which a curve twists and coils around itself" [34,37]. The writhe number was normally used as a factor to discriminate between healthy vessels and vessels with aneurysms. In the former case, the writhe number is zero as healthy vessels are modeled essentially as tubular structures. However, when the writhe number is nonzero the blood vessel is reported as containing a possible aneurysm. Lauric et al. [34] analyzed the distribution of the writhe number values along the whole surface of an aneurysm, and concluded that ruptured aneurysms tend to have regions with high writhe number values.

Additionally, Raghavan et al. [31] proposed various indices to characterize the shape and size of saccular aneurysms and their relation to the risk of rupture based on a study with 27 patients with ruptured and unruptured aneurysms. They found that the lesion's nonsphericity index (NSI), undulation index (UI), and ellipticity quantified by either the ellipticity index (EI) or the aspect ratio (AR) were the best predictors of rupture risk. The relations between these indices, those of Parlea et al. [32] and the associated risk of rupture are listed in Table 1 of Raghavan et al. [31]. They are not discussed here as they are beyond the scope of this review.

Moreover, Tremmel et al. [38] suggested another important parameter called aneurysm-to-parent vessel size ratio (SR), defined as the maximum aneurysm height/average parent vessel diameter, incorporating the parent vessel geometry into a morphological index. They set the average parent vessel diameter at 2.5 mm for intracranial aneurysms and concluded that SR has a significant effect on intracranial aneurysm hemodynamics. They showed that values of SR < 2 led to simple flow patterns with a single intraneurysmal vortex (strongly correlated with low rupture risk), whereas SR > 2 presented multiple vortices and complex flow patterns (strongly correlated with high rupture risk). Even though all these indices were able to predict the risk of rupture in a large number of patients, it is still unclear about the causes of rupture, and more clinical trials are required to validate these methods.

many places in the brain, and in particular at the basilar bifurcation, middle cerebral artery (MCA), anterior communicating (AcomA), posterior communicating (PcomA), superior cerebellar (SCA), and posterior cerebral (PCA) arteries, Parlea et al. [32] concluded that the most common saccular aneurysms have a quasi-spherical shape with $D/H \approx 1.1$ and $H/S \approx 1.98$. In terms of absolute sizes, the dimensions of aneurysms vary between 2.81 and 5.72 mm for H, between 3.08 and 6.99 mm for D and between 2.06 and 6.66 mm for the neck diameter, depending on the location and development stage of the aneurysms [33]. Lauric et al. [34] reported similar size and shape indices as Parlea et al. [32] and others [35,36], and in addition introduced the *writhe number* proposed by Fuller [37] as a method to analyze the shape of the saccular aneurysms and to predict their rupture status by means of the aneurysm dimensions (height, width, and neck diameter). The writhe number, defined as a geometric invariant of a space curve,

2.3   Influence of Hemodynamic Factors in Aneurysms. The hemodynamic factors play a fundamental role in the formation, growth, and rupture of cerebral aneurysms, but today it is still unclear whether they are uniquely responsible for this pathology or just one of a combination of factors including degenerative biological processes (i.e., consequence of biochemical or structural disorders, diseases, or ageing) [26]. In particular, the

Table 1   Proposed hemodynamic indices to evaluate the probability of aneurysm initiation

Index	Definition	
WSS (wall shear stress)	$\boldsymbol{\tau}(t) = -\mu[\partial \mathbf{u}(t)/\partial \mathbf{n}]\vert_{wall}$	μ is the blood viscosity, $u(t)$ is the fluid velocity parallel to the wall, and $\mathbf{n}$ is the outer unit vector normal to the vessel wall [39]
Mean WSS (mean wall shear stress)	$\overline{\tau(t)} = (1/T)\int_0^T \tau(t)dt$	
SWSSG (spatial wall shear stress gradient)	$\mathbf{G} = \nabla\vert\boldsymbol{\tau}(t)\vert$	
OSI (oscillatory shear index)	$\frac{1}{2}\left\{1 - \left[(T\vert\overline{\tau(t)}\vert)/\left(\int_0^T \vert\tau(t)\vert dt\right)\right]\right\}$	T is the period of the cardiac cycle [39]
AFI (aneurysm formation indicator)	$\cos\theta = \left[\boldsymbol{\tau}(t)\cdot\overline{\tau(t)}/\|\boldsymbol{\tau}(t)\|\cdot\|\overline{\tau(t)}\|\right]$	Quantifies the change in direction of WSS [40]
GON (gradient oscillatory number)	$1 - \left(\left\vert\int_0^T \mathbf{G}dt\right\vert/\int_0^T \vert\mathbf{G}\vert dt\right)\ (0 \le GON \le 1)$	The integration is calculated over one pulse period T. [41]
IMI (impingement index)	$-(\partial\boldsymbol{\sigma}/\partial y)/(\bar{\tau}/R)$	$\bar{\tau}$ is the mean wall shear at the entrance of the artery, R the radius of the internal carotid artery, $\boldsymbol{\sigma}$ is the normal stress and y indicates the n direction [42]

causes for the initiation of the aneurysms are still not well understood [27] and therefore its prediction is currently very difficult.

CFD advances in the last decades have provided useful tools to clarify the effect of fluid dynamics in cerebral aneurysms, and led to the appearance of various hemodynamic indices for detecting aneurysm initiation (these indices are summarized in Table 1), which are different from the size and shape indices discussed in Sec. 2.2. Ku et al. [39] proposed the oscillatory shear index (OSI) as a numerical parameter to quantify the shear stress imposed on the arterial wall in pulsatile flow, and also with the purpose of providing an index "to describe the shear stress acting in directions other than the direction of the time-averaged shear stress vector." A value close to 0.5 represents strong WSS direction changes, while a zero value indicates no change [43]. At this point, it is important to emphasize that the shear stress imposed on the arterial wall is a traction force, which is a force with normal and tangential components. The WSS is calculated from the traction vector, $\mathbf{T}$, which is defined from the stress tensor (τ) as $\mathbf{T} = \tau \cdot \mathbf{n}$. Therefore, the WSS is the viscous force working parallel to the arterial wall, the tangential component of the traction vector expressed as $\mathrm{WSS} = \mathbf{T} - (\mathbf{T} \cdot \mathbf{n})\mathbf{n}$.

The potential aneurysm formation indicator (AFI) was proposed by Mantha et al. [40] and takes into account "the alignment of the WSS vector with endothelial cells over the course of the cardiac cycle" (large values of AFI), since it is accepted that the endothelial cells are preferentially aligned in the direction of the time-averaged WSS vector. It was found that the stagnation zones detected by AFI (low values of AFI) coincide with aneurysm locations, which demonstrates the usefulness of this index in the study of the aneurysms formation. Shimogonya et al. [41] suggested the gradient oscillatory number (GON), which analyzes the temporal fluctuations of the spatial gradient of the WSS vector (SWSSG). It is designed to quantify the disturbance intensity of hemodynamic forces acting on the wall surface (a higher GON for an increased disturbance). The recent numerical work of Kojima et al. [44] for pulsatile flow conditions, aimed to determine an effective index for aneurysm growth, and concluded that aneurysms grow in regions with low wall shear stresses, low values of AFI, and high OSI. More recently, Jou and Mawad [42] defined an impingement index (IMI) "to assess the timing and size of flow impingement in the case of a giant carotid aneurysm." This new index is closely related with the WSSG since it has a similar definition to WSSG, except that IMI also provides the direction of the shear stress. Nevertheless, acceptable ranges for GON, AFI, and IMI have not yet been experimentally determined and this is an area where more investigation is clearly needed.

In spite of the wealth of indices to evaluate the aneurysm initiation and its subsequent risk of rupture, the literature is scarce on investigations of the growth process. According to Sforza et al. [27], it is still unclear what are the mechanisms that are responsible for the growth of cerebral aneurysms, and they reported two possible main mechanisms with a common factor, the weakening of the arterial wall of the aneurysm. Those two mechanisms are referred to as the high-flow effects and the low-flow effects mechanisms. The former is related to an endothelial injury with wall remodeling and degeneration as a result of a high WSS [45,46]. In contrast, the second theory is based on a localized blood-flow stagnation region in the dome of the aneurysm caused by a slow flow within the aneurysm, which could lead to the progressive thinning and subsequent tear of the aneurysm vessel wall. Recently, Tanoue et al. [47] evaluated the hemodynamic changes during the growth process of aneurysms and revealed the presence of high WSSG in the surroundings of the aneurysm growth region and very low WSS at the growth region. Other studies also reported correlations between the low WSS and aneurysm growth [48–50].

However, very few studies related to the rupture of aneurysms have been carried out, mainly due to the difficulty in getting (in vivo) data under such extreme and dangerous conditions.

Overall, there is a clear lack of consensus about the hemodynamic factors involved in the initiation, growth, and rupture of cerebral aneurysms; hence, finding a reliable and accurate method to calculate the risk of rupture is a challenging objective in which fluid mechanics in combination with tissue mechanics plays a vital role. Therefore, it comes as no surprise that over the last decade a large number of investigations have been addressing these issues from all relevant perspectives, i.e., in vivo and in vitro clinical techniques, as well as experimental and numerical modeling of the hemodynamics of cerebral aneurysms. In the latter case, the mechanics of soft materials and biology become essential components. However, looking exclusively into the fluid mechanics of this complex problem to select a proper mathematical model, that is able to describe the flow behavior of real human blood is already a major challenge and would mean a significant step forward. The fluid mechanics aspect is the focus of the remainder of this review, and will be discussed in detail in the Secs. 3, 4, and 5.

3 CFD Methodology

The most common modeling technique used to perform hemodynamic numerical simulations is CFD based on a continuum approach, described by the Navier–Stokes equations. The governing equations used in flow dynamics are expressed as

$$\nabla \cdot \mathbf{v} = 0 \tag{1}$$

$$\rho \left(\frac{\partial \mathbf{v}}{\partial t} + \mathbf{v} \cdot \nabla \mathbf{v} \right) = -\nabla p + \nabla \cdot \tau \tag{2}$$

where ρ is the fluid density, $\mathbf{v}$ is the velocity vector, p is the pressure, and τ is the extra-stress tensor. These need to be solved together with an appropriate constitutive equation describing the fluid rheology (as discussed below in Sec. 3.1).

For a Newtonian fluid, the extra-stress tensor can be expressed as $\tau = 2\mu\mathbf{D}$, where $\mathbf{D}$ is the strain rate tensor $\mathbf{D} \equiv (\nabla\mathbf{v} + (\nabla\mathbf{v})^{\mathrm{T}})/2$ and the scalar μ is the constant viscosity coefficient [15]. For non-Newtonian fluids, more complex constitutive relations are needed (see Sec. 3.1) and in their simplest form (the Generalized Newtonian fluid model) the viscosity is no longer constant but depends on the second and third invariants of $\mathbf{D}$. The solution of this set of equations yields a description of the flow at a given point in space and time.

Once the governing equations are selected and a suitable constitutive equation (rheological model) for blood is chosen, the boundary conditions (BCs) must be taken into account. These BCs are the inlet velocity profile, entry and exit conditions regarding pressure and the flow conditions at the wall in terms of velocity and pressure. The mechanical properties of the arterial wall are also needed together with an adequate description of the wall position (Fig. 3). Some of these aspects are discussed in more detail in Sec. 3.3.

3.1 Rheological Constitutive Equations for Blood. It is well known that blood exhibits rheological properties such as viscoelasticity, shear-thinning, thixotropy, and yield stress [10,11,16]. This complex behavior is influenced by such factors as plasma viscosity, level of hematocrit, and level of aggregation of RBCs (rouleaux) among others. In terms of blood rheology, the behavior under steady shear flow is arguably the most well studied experimentally, with the viscosity curve for whole human blood exhibiting shear-thinning at intermediate shear rates and a Newtonian plateau region at high shear rates (Fig. 4(a)). In addition, a yield stress value around 1.5–5 mPa, which increases with the hematocrit, has been measured experimentally [52]. Apart from the steady shear viscosity, other material properties in oscillatory shear flows have also been analyzed. For instance, Vlastos et al. [53] determined the elastic and viscous components of the complex viscosity by means of a viscometer, Sousa et al. [54] used large amplitude oscillatory shear to assess its nonlinear response, and Campo-Deano et al. [16] obtained the viscoelastic moduli G'
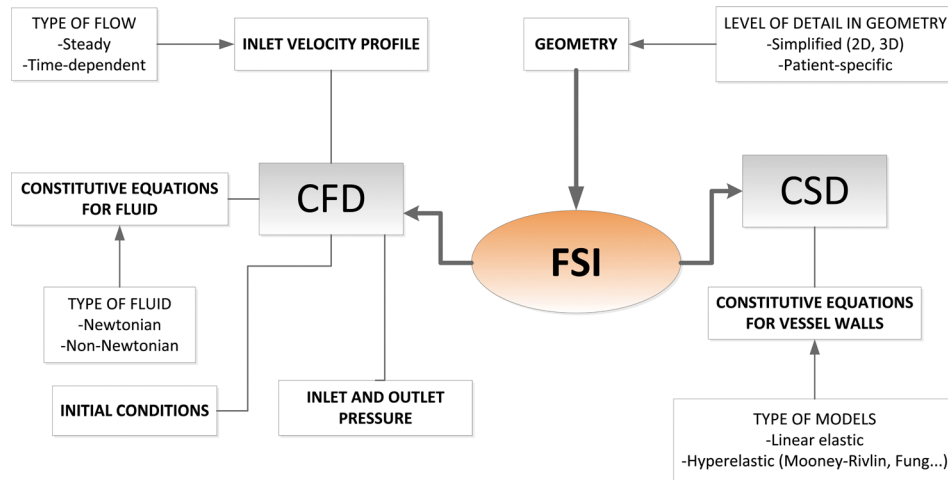
Fig. 3 Schematic representation of the main processes in handling computational hemodynamics
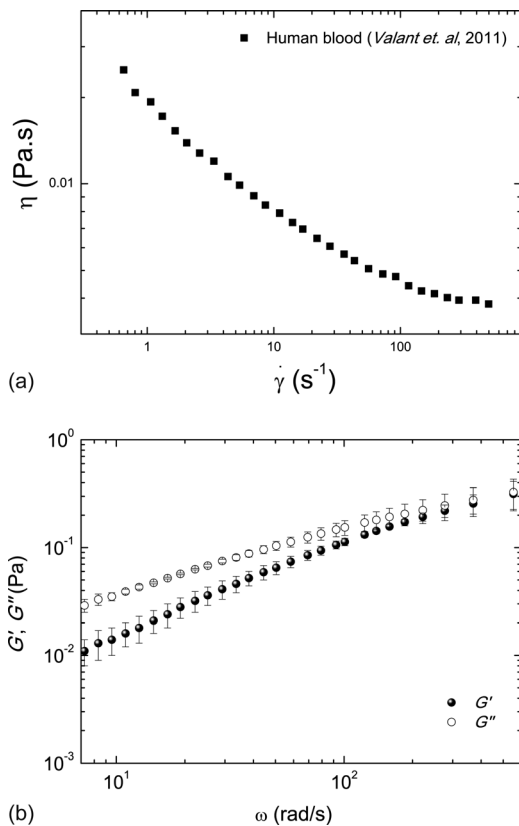

(a)

(b)

Fig. 4 Shear rheology of whole blood measured experimentally. (*a*) Steady shear viscosity (*η*) curve [51]. (*b*) Storage (solid circles) and loss (open circles) moduli (adapted from Campo-Deano et al. [16]).
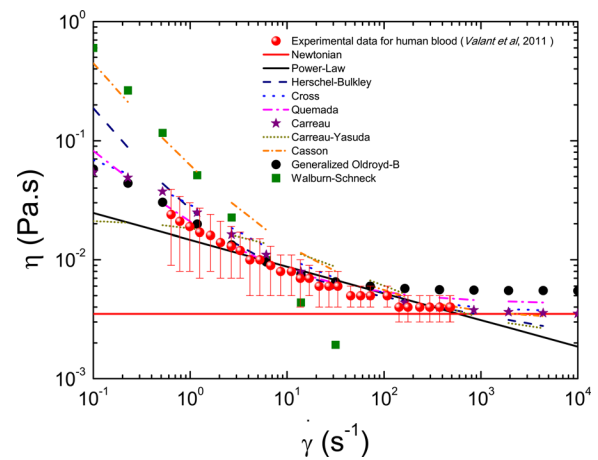

Fig. 5 Average viscosity of whole blood measured experimentally by Valant et al. [51], compared to the different constitutive models described in Table 2. The experimental viscosity values are an average over blood samples of Hct ranging between 36% and 49%. The error bars correspond to the standard deviation of the averaged viscosity values.

(storage modulus) and G'' (loss modulus) performing passive microrheology experiments. Even though the storage and loss moduli (Fig. 4(*b*)) clearly indicate a liquidlike behavior—G'' is larger than G' [16]—the difference is not so large especially at high frequencies, and this confirms that there is a non-negligible elastic contribution to the bulk rheology of blood. As explained in Sec. 1, the role of elasticity will be emphasized in small vessels where cerebral aneurysms are typically found.

In CFD simulations reported in the literature, different levels of simplification have been considered to describe the blood rheology, and therefore a range of different models have been used over the last decades, ranging from simple Newtonian and Generalized-Newtonian models to more complex non-Newtonian viscoelastic models.

Figure 5 compares an experimental measurement of the steady shear viscosity of human blood with the viscosity curves for the most commonly considered non-Newtonian models, as discussed below. The rheological behavior of human blood can be considered Newtonian when the shear rate is high enough, so that internal structures such as rouleaux do not exist. This high constant shear viscosity of human blood, corresponding to the high shear rate plateau (η_∞), is accepted to be in the range from 3.5 mPa·s to 5 mPa·s according to different authors, such as Anand and Rajagopal [60] and Bodnar et al. [62]. The value of the shear rate above which blood flow can be considered Newtonian has been shown to vary depending on factors such as the level of hematocrit [63]: Eckmann et al. [8] set this limit at $45\,\mathrm{s}^{-1}$, Stuart and

Table 2 Viscosity models for human blood to be used in the context of the generalized Newtonian fluid model

Model	Constitutive equation[a]
Casson	$\eta = (1/\dot{\gamma})[K_0(c) + K_1(c)\sqrt{\dot{\gamma}}]^2$
	$K_0(c) = 0.1937$ (Pa)$^{1/2}$, $K_1(c) = 0.055$ (Pa·s)$^{1/2}$ [55]
Walburn–Schneck	$\eta = C_1 e^{(C_2 + C_3/H^2)}|\dot{\gamma}|^{(1-C_4 H)}$
	$C_1 = 0.00797$ Pa·s, $C_2 = 0.0608$, $C_3 = 377.7515$, $C_4 = 0.00499$ [56]
Power-law	$\eta = k\dot{\gamma}^{n-1}$
	$k = 14.67.10^{-3}$ N s^n/m^2, $n = 0.7755$ [57]
Herschel–Bulkley	$\eta = k\dot{\gamma}^{n-1} + (\tau_0/\dot{\gamma})$
	$k = 8.9721.10^{-3}$ N s^n/m^2, $n = 0.8601$, $\tau_0 = 0.0175$ N/m^2 [58]
Carreau	$\eta(\dot{\gamma}) = \eta_\infty + (\eta_0 - \eta_\infty)[1 + (\lambda\dot{\gamma})^2]^{(n-1)/2}$
	$\eta_0 = 0.056$ Pa·s, $\eta_\infty = 0.00345$ Pa·s, $n = 0.3568$, $\lambda = 3.313$ s [59]
Carreau–Yasuda	$\eta(\dot{\gamma}) = \eta_\infty + (\eta_0 - \eta_\infty)[1 + (\lambda\dot{\gamma})^a]^{(n-1)/a}$
	$\eta_0 = 0.022$ Pa·s, $\eta_\infty = 0.0022$ Pa·s, $a = 0.644$, $n = 0.392$, $\lambda = 0.110$ s [19]
Modified generalized Oldroyd-B	$\eta = \eta_\infty + (\eta_0 - \eta_\infty)[(1 + \ln(1 + \Lambda\dot{\gamma}))/(1 + \Lambda\dot{\gamma})]$
	$\eta_\infty = 0.0055$ Pa·s, $\eta_0 = 0.0736$ Pa·s, $\Lambda = 14.81$ s [60]
Quemada	$\eta = \eta_\infty \left[1 - (1/2)\left(K_0 + K_\infty \sqrt{\dot{\gamma}/\dot{\gamma}_c}/\left(1 + \sqrt{\dot{\gamma}/\dot{\gamma}_c}\right)\varphi\right]^{-2}\right.$
	$\eta_\infty = 0.0012$ Pa·s, $\dot{\gamma}_c = 1.88$ s^{-1}, $k_\infty = 2.07$, $k_0 = 4.33$, $\varphi = 0.45$ [61]
Cross	$\eta = \eta_\infty + (\eta_0 - \eta_\infty)/(1 + (\lambda\dot{\gamma})^n)$
	$\eta_0 = 0.126$ Pa·s, $\eta_\infty = 0.0036$ Pa·s, $n = 0.64$, $\lambda = 8.2$ s [62]

[a]$\dot{\gamma}$ is the shear rate with units s^{-1}, which is the scalar invariant of the strain rate tensor $\dot{\gamma}_{ij} = (\partial/\partial x_i)v_j + (\partial/\partial x_j)v_i$, then $\dot{\gamma} = \sqrt{(1/2)\sum_i \sum_j \dot{\gamma}_{ij}\dot{\gamma}_{ji}}$. η_0 and η_∞ are the low shear rate and the high shear rate constant viscosities, respectively. λ is the characteristic time constant.

Kenny [64] at $50\,\text{s}^{-1}$ and others state that this limit is in the range of 100–$300\,\text{s}^{-1}$ [9].

In large vessels, the shear rate can vary between 0 and $1000\,\text{s}^{-1}$ along one pulse of the cardiac cycle, i.e., covering a wide range of shear rates where the blood viscosity exhibits a variety of behaviors [63]. Moreover, low shear rate regions appear in some vessel sections such as near bifurcations, graft anastomoses, stenosis, and aneurysms [63]. Nevertheless, in small vessels the elastic effects are emphasized as explained previously, rendering inadequate the use of Newtonian models.

A number of models consider a Newtonian plateau region also at low shear rates, while others take into account the existence of a yield stress, as is the case of the Herschel–Bulkley and the Casson models. For shear stresses below the critical yield value, there will be no velocity gradients and the fluid will move as a solid body with a constant velocity [65] except near the vessel walls in which there is flow, because the stresses exceed the yield value (if the stress is everywhere below the yield value there will be no flow). The power-law and the Walburn–Schneck models are viscosity functions that fit just the intermediate shear-thinning region [56], while others, such as the models of Quemada, Cross, Carreau, Carreau-Yasuda, and a generalization of the Oldroyd-B model can additionally capture the two Newtonian plateau regions. These non-Newtonian models are detailed in Table 2.

Apart from these models, other non-Newtonian constitutive equations that take into consideration the blood viscoelasticity and thixotropy were proposed in the literature. The need for viscoelastic models arises from the strong link between the blood structure and the fluid rheology. The viscoelastic character of blood is due to both the deformation of individual RBCs and the formation and disruption of aggregates of RBCs in the flow. The dynamics of rouleaux involve the storage and release of elastic energy, as well as the dissipation of energy in the blood due to the evolution of RBCs, its networks, and internal friction.

In 1979, Thurston [10] proposed one of the first viscoelastic models of blood inspired on a generalized Maxwell model showing thixotropy, viscoelasticity, and shear-thinning. More recently,

Owens [20] proposed a constitutive equation for whole human blood (Table 3) that is able to link the blood rheology with the aggregation/disruption of erythrocyte structures at different shear rates. This model showed good agreement with experimental data from the simple triangular step shear rate experiment of Bureau et al. [68]. Later, Moyers-Gonzalez et al. [21] presented a nonhomogeneous model for whole human blood (also shown in Table 3) based on the previous model of Owens [20], in which they considered stress-induced diffusion of the cells in addition to the formation and destruction mechanisms of rouleaux. Other non-Newtonian viscoelastic models such as the Giesekus, sPTT [16], Oldroyd-B or Generalized Oldroyd-B models [67,69] were successfully used to mimic the rheological behavior of blood in steady and oscillatory flows, and used to numerically predict the flow in vascular conditions representing diseased vessels with moderate success (Bodnar et al. [62], and Javadzadegan et al. [70]). These rheological models work in the high-strain or high-strain rate (nonlinear viscoelastic) regimes and are able to predict shear-thinning behavior as well as reasonable normal-stress effects.

Another class of blood rheology models was developed within a thermodynamic framework by Anand and Rajagopal [60], in which blood is characterized by four independent parameters reflecting the elasticity, the viscosity of the plasma, the dynamics of rouleaux, and their effects on the shear thinning behavior of the viscosity that takes place during the flow. This model was shown to be in good agreement with experimental data in steady Poiseuille flow and oscillatory shear flow [71].

Besides the rheological behavior of whole blood, it is important to analyze other factors required to perform meaningful numerical simulations, such as inlet velocity profiles, outlet BCs or the viscoelasticity of arterial walls. In Secs. 3.2 and 3.3, we will discuss these issues in more detail.

3.2 BCs. To carry out CFD simulations, the BC of all computational domains must be formulated, as they are an essential component of the mathematical model and play a very

Table 3 Non-Newtonian mathematical models for human blood exhibiting viscoelasticity. Structured models.

Model	Constitutive equation
Thurston [10]	$\boldsymbol{\tau} = \sum\limits_{j=1}^{6} \tau_j + 2\eta_\infty \mathbf{D}$ $\tau_j + \lambda_j(\partial \tau_j/\partial t) = 2\left(\eta_{o,j}/(1+(\lambda_j \gamma)^2)\right)D$ $\eta = \eta_\infty + \sum\limits_{j=1}^{6} \eta_{o,j}\left[1+(\lambda_j\gamma)^2\right]^{-1}$
Owens [20][a]	$\boldsymbol{\tau} + \mu(\partial\tau/\partial t - \nabla\boldsymbol{v}\cdot\boldsymbol{\tau} - \boldsymbol{\tau}\cdot\nabla\boldsymbol{v}^T) = N_0 k_B T \mu\dot{\boldsymbol{\gamma}}$ $\mu = (n\lambda_H/1 + g_n n\lambda_H)$ $(dn/dt) = -(1/2)[b(\dot\gamma)(n-n_{st})(n+n_{st}-1)]$ $b(\dot\gamma) = a(\dot\gamma)N_0/[n_{st}(n_{st}-1)]$ $n_{st} = (\eta_0/\eta_\infty)(1+\Phi\dot\gamma^m)/(1+\beta\dot\gamma^m)(1+(3/2)a(\dot\gamma)N_0\lambda_H)$
Moyers-Gonzalez et al. [21][b]	$(DN_0/Dt) = D_{tr}\nabla^2 N_0 - (D_{tr}/(k_B T + \kappa))\nabla\nabla : \boldsymbol{\tau}$ $\boldsymbol{\tau} + \bar\mu \overset{\nabla}{\boldsymbol{\tau}} -D_{tr}\bar\mu(\nabla^2\boldsymbol{\tau} + (\nabla\nabla:\boldsymbol{\tau})\boldsymbol{\delta}) = N_0(k_B T + \kappa)\bar\mu\dot{\boldsymbol{\gamma}}$ $(DM/Dt) = D_{tr}\nabla^2 M - (D_{tr}/(k_B T + \kappa))\nabla\nabla : \boldsymbol{\sigma} - (a(\dot\gamma)/2)M^2 + (b(\dot\gamma)/2)(N_0 - M)$ $\boldsymbol{\sigma} + \bar\mu \overset{\nabla}{\boldsymbol{\sigma}} -D_{tr}\bar\mu(\nabla^2\boldsymbol{\sigma} + (\nabla\nabla:\boldsymbol{\sigma})\boldsymbol{\delta}) = M(k_B T + \kappa)\bar\mu\dot{\boldsymbol{\gamma}}$
Anand and Rajagopal [60][c]	$\boldsymbol{\sigma} = -p\boldsymbol{I} + \mathbf{S}$ $\mathbf{S} = \mu\mathbf{B}_{k_{p(t)}} + \eta_1\mathbf{D}$ $\mathbf{B}_{k_{p(t)}} = -2((\mu/\alpha))^{1+2n}(\text{tr}(\mathbf{B}_{k_{p(t)}}) - 3\lambda)^n[\mathbf{B}_{k_{p(t)}} - \lambda\boldsymbol{I}]$ $\lambda = \left[3/\text{tr}(\mathbf{B}_{k_{p(t)}}^{-1})\right]$ $n = (\gamma - 1)/(1 - 2\gamma); n > 0$
Giesekus [66]	$\boldsymbol{\tau}_p + \lambda \overset{\nabla}{\boldsymbol{\tau}_p} +\alpha(\lambda/\eta_0)\boldsymbol{\tau}_p\boldsymbol{\tau}_p = -\eta_0\dot{\boldsymbol{\gamma}}$
PTT [67]	$\Upsilon(tr\boldsymbol{\tau}_p)\boldsymbol{\tau}_p + \lambda \overset{\nabla}{\boldsymbol{\tau}_p} +(\xi/2)\lambda(\dot{\boldsymbol{\gamma}}\boldsymbol{\tau}_p + \boldsymbol{\tau}_p\dot{\boldsymbol{\gamma}}) = \eta_0\dot{\boldsymbol{\gamma}}$

[a]N_0: number of red blood cells per unit volume; n: average aggregate size; n_{st}: steady state value of n at a given shear rate$(\dot\gamma)$; a$(\dot\gamma)$: aggregation rate; b$(\dot\gamma)$: disaggregation rate; β, Φ: Cross model parameters; λ_H: Maxwell relaxation time; and $g_n n = (1/2)bn(n-1) + aN_0$. T is the absolute temperature

[b]D_{tr}: translational diffusivity; $\bar\mu$: averaged relaxation time; κ: constant which takes account of impacts with other blood cells; and M: number density of the rouleaux.

[c]$\mathbf{B}_{k_{p(t)}}$: Left Cauchy–Green stretch tensor calculated using $\mathbf{k}_{p(t)}(\mathbf{B})$ (stress-free configuration reached by instantaneously unloading the body) as the reference configuration; $\boldsymbol{\sigma}$: Cauchy stress tensor.

important role in the performance of computational analysis in cerebral aneurysms. On the arterial/vessel walls, the no-slip and no-penetration conditions are applied when the wall is considered inelastic. On the contrary, if we consider the mechanical properties of the arterial wall, the problem becomes more complex and FSI must be applied (FSI will be discussed in Sec. 3.3). Often, symmetry BCs are applied to reduce the computational effort in a problem. In this case, the flow field and the geometry must be symmetric. The BCs related to inlets and outlets are explained in detail in Secs. 3.2.1 and 3.2.2.

3.2.1 Inlet BCs. Selecting suitable inlet time-dependent velocity conditions is a crucial issue when performing computational hemodynamic studies. During a cardiac cycle, it is possible to distinguish between diastole, during which the ventricles are filling with blood and systole, during which the ventricles are actively contracting and pumping blood out of the heart and into the main arteries. Consequently, blood flow is unsteady, showing pulsatile conditions in all arteries, which have characteristic pulsatile profiles that depend on the local pressure wave and wall compliance [52,72,73]. In fact, it is possible to compare the pulses near the heart and in cerebral vasculature, showing that the velocity decreases as we move away from the heart (Fig. 6). For example, the average flow velocities in the MCA are approximately 80 cm/s with systolic peaks of 120 cm/s, while near the heart they are of the order of 80 cm/s with systolic peaks of 160 cm/s [74].

In computational hemodynamics, only parts of arteries or of the circulatory system are usually modeled, and the two typical velocity fields used are steady flow [52], with average velocity values depending on the vessel being studied, and pulsatile flow. When a

CFD study is carried out and no patient-specific data is available (patient-specific BCs), idealized inlet velocity profiles are defined. The blunt profile and the parabolic profile are the most commonly used inlet velocity profiles for steady flow studies and can be expressed as

$$v = \frac{\gamma+2}{\gamma}V\left[1 - \left(\frac{r}{R}\right)^\gamma\right] \qquad (3)$$

where V is the average velocity, v is the local velocity at the radial position r, R is the radius of the cylindrical vessel, and γ is a constant parameter defining the profile bluntness for a particular profile.

For $\gamma = 2$ a fully developed parabolic flow is recovered, while higher values of γ correspond to a more pluglike velocity profile. For the cardiac cycle a value of 9 was found suitable to mimic the blood flow velocity profile. This value is the result of a fit from experimental data obtained at different points in the cardiac cycle [75].

When the flow is unsteady, apart from the shape of the inlet velocity profile, the velocity waveform should also be defined. The Womersley profile for unsteady flow formulations is generally the most widely used [76] and for fully developed pulsatile flow of an incompressible Newtonian fluid in a straight tube of radius R it can be expressed as

$$v = \frac{A}{\rho}\frac{1}{i\omega}\left\{1 - \frac{J_0\left(r\sqrt{\frac{\omega}{\nu}}i^{3/2}\right)}{J_0\left(R\sqrt{\frac{\omega}{\nu}}i^{3/2}\right)}\right\} \qquad (4)$$
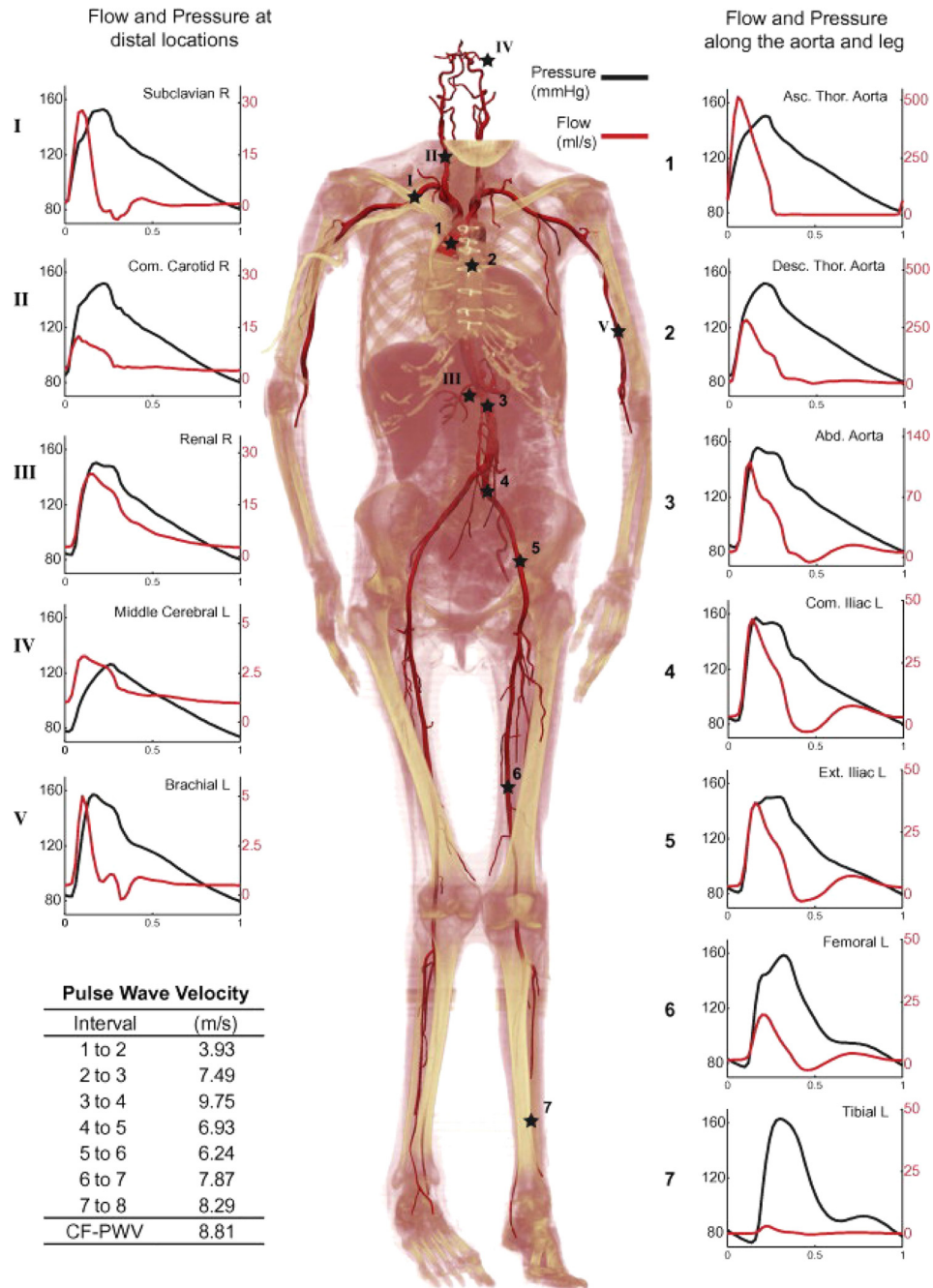
Fig. 6 Pressure and flow waves at multiple sites in the full body model. (Reprinted with permission from Xiao, et al. [74]. Copyright 2013 Elsevier).

in which ν is the kinematic viscosity, ω is the angular frequency, $J_0(xi^{3/2})$ is a Bessel function of order zero and complex argument, and $R\sqrt{(\omega/\nu)} = \alpha$ is a dimensionless parameter known as the Womersley number, which is the ratio of inertial forces relative to viscous forces and is used to characterize the pulsatile flow of a Newtonian fluid within an artery.

The Womersley number is used to transform a steady profile (e.g., the parabolic and blunt profiles of Eq. (3)) into an unsteady profile. In order to do that, the corresponding velocity profile should be multiplied by a function of time, with the frequency being derived from the appropriate Womersley number. Based on Eq. (3), the temporal and spatial velocity distribution in the case of pulsatile flow is as follows:

with

$$v = 2V\left[1 - \left(\frac{r}{R}\right)^2\right] + \sum V_n \left[\frac{1 - \frac{J_0\left(\beta_n \frac{r}{R}\right)}{J_0(\beta_n)}}{1 - \frac{2J_1(\beta_n)}{\beta_n J_0(\beta_n)}}\right] e^{in\omega t} \quad (5)$$

$$\beta_n = i^{\frac{3}{2}}\alpha_n = i^{\frac{3}{2}}R\sqrt{\frac{n\omega}{\nu}} \quad (6)$$

The Womersley number can vary significantly along the cardio-vascular system. For instance, Fung [77] stated that at rest the value of α in the ascending aorta is approximately equal to 13.2, dropping to 4.4 in the carotid artery, and can be further reduced to 0.005 inside the capillaries, where inertial forces become less important and the flow is determined by the balance of viscous stresses and the pressure gradient [78].

Campbell et al. [79] carried out a study to analyze the effect of the inlet velocity profile in pulsatile CFD simulations of the flow inside the carotid bifurcation. They evaluated the three previously mentioned inlet velocity profiles against the patient-specific velocity profile and concluded that the parabolic inlet velocity profile resulted in values of the mean WSS and OSI similar to simulations using the real patient-specific inlet velocity profile. Nevertheless, it was found that the inlet velocity profile is not such a decisive factor affecting the values of WSS or OSI as the change in the morphology of the vessel or even the use of an alternative waveform.

3.2.2 Outlet BCs. Another important BC is the outlet velocity/pressure. In computational problems related with arterial flow and specifically involving multiple outlets, outflow BCs in domains may also lead to a variation of local features such as WSS even at regions located far away from the terminal vessels [80,81]. There are several methods for the outlet BC:

— The *open BC*, originally proposed by Papanastasiou et al. [82], is the most suitable method for truncated domains where the outflow BCs are unknown. Subsequently, other authors have implemented this BC [83–85] and it was also tested successfully by Park and Lee [86] with viscoelastic models.
— The *zero pressure outlet* BC is the most widely used [18]. However, this condition is not the most suitable in the case of hemodynamics studies since it considers atmospheric air conditions at the end of the vessel, neglecting any change in the pressure and flow rate as a consequence of the influence of the downstream vessels [87].
— The *resistance BC* is a standard BC commonly used [88–90]. It takes into consideration a linear relation between flow rate and pressure at the outlets and is equivalent to imposing a constant pressure gradient for steady flow simulations.
— The *Windkessel model BC* is a BC to be exclusively used in the context of the lumped parameter heart model that represents blood flow and pressure in the systemic arteries of the whole body (or large parts of the body) using simplified equations. The most common lumped parameter model is the three-element Windkessel model (RCR) introduced by Westerhof et al. [91]. It can be derived from electrical circuit analogies with two resistors in sequence with a capacitor, where the current represents arterial blood flow, voltage represents arterial pressure, resistances (R) represent arterial and peripheral resistance that occur as a result of viscous dissipation inside the vessels and capacitors (C) represent volume compliance of the vessels that allows them to store large amounts of blood [92], i.e., the model incorporates also vessel deformability. It can be applied to both steady and unsteady flow simulations [93,94].
— The *impedance BC* is another BC specific to a model, in this case approximating the arterial network as a 1D treelike structure, with linearized flow equations that can be solved analytically, and incorporating time-periodicity of the flow. The model can be 1D, 2D, or three-dimensional (3D) and the flow domain can have multiple outlets. The method needs several cardiac cycles to achieve convergence of the results and therefore it leads to an expensive simulation.

3.3 Viscoelastic Properties of the Arterial Wall. Modeling the FSI between the blood flow and the vessel walls is of great
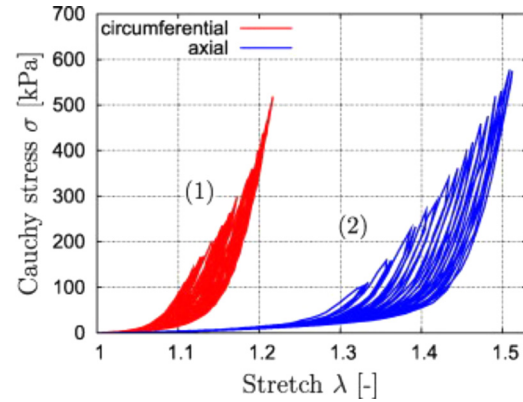
Fig. 7 Cyclic uniaxial tension tests of the media of a human carotid artery in circumferential (1) and axial (2) directions. (Reprinted with permission from Balzani, D., et al. [98] Copyright 2012 Elsevier).

importance in studies related with hemodynamics in the human circulatory system, since the mechanical properties of the arteries play a very important role and are at the origin of several cardiovascular complications and events like aneurysm formation and rupture [95,96]. Some studies have shown that the elastic properties of the arterial walls are strongly related with the arterial pressure, which translates into a variation of the stiffness of the arterial walls during the cardiac cycle [97]. Rourke et al. [95] surveyed the methods and quantities used to estimate the arterial stiffness. They listed eleven different indices of arterial stiffness, including the 'arterial compliance', "Young's modulus" or "elasticity index," and in addition provided reference values for these indices for healthy and diseased arteries. The interested reader is referred to Tables 1 and 2 of Ref. [95] for a complete list. The typical stress/strain curve of a human artery is shown in Fig. 7. These curves were obtained experimentally by Balzani et al. [98] in the circumferential and the axial directions, and show a strong anisotropy and a pronounced softening hysteresis. In order to reproduce this behavior, different models for the arterial walls need to be defined and subsequently coupled with the fluid domain (CFD) to account for FSI.

3.3.1 Computational Structure Dynamics (CSD). The governing equations for the structural mechanics of the vessel walls are the equilibrium equations [99]

$$\rho^s \left(\frac{d^2 \mathbf{y}}{dt^2} + \varepsilon \frac{d\mathbf{y}}{dt} - \mathbf{f}^s \right) - \nabla \cdot \boldsymbol{\sigma}^s = 0 \qquad (7)$$

where $\mathbf{y}$ is the structural displacement vector, $\mathbf{f}^s$ is the external body force acting on the structure, ρ^s is the density of the tissue material, ε is an artificial-damping coefficient, and $\boldsymbol{\sigma}^s$ is the Cauchy stress tensor with s denoting the structure (to distinguish it from the fluid stress tensor). The Cauchy stress is expressed in terms of the second Piola–Kirchoff stress tensor $\mathbf{S}$ through the kinematic transformation ($\mathbf{S} = J\mathbf{F}^{-1} \cdot \boldsymbol{\sigma}^s \cdot \mathbf{F}^{-T}$, where $\mathbf{F}$ is the deformation gradient and $J = \det \boldsymbol{F}$ is the Jacobian determinant). The differences between models of the arterial structure lay in the definition of $\mathbf{S}$.

In the case of linearly elastic materials, $\mathbf{S}$ (in indical notation) is defined by

$$S^{ij} = \left(\lambda^{-s} G^{ij} G^{kl} + \mu^s \left(G^{il} G^{jk} + G^{ik} G^{jl} \right) \right) E_{kl} \qquad (8)$$

where λ^s and μ^s are the Lamé constants, G^{ij} is the contravariant metric tensor in the undeformed configuration, and E_{kl} is the Cauchy–Green strain tensor [100].

The two most common hyperelastic models are the Fung [101] and the Mooney–Rivlin [102,103] models, which are based on phenomenological descriptions of observed behavior of different materials. In the former, S^{ij} is defined by

$$S^{ij} = 2D_1 D_2 e^{D_2(I_1-3)} G^{ij} + \left(K_{\text{PEN}} ln\left(\sqrt{I_3}\right) - 2D_1 D_2\right) g^{ij} \quad (9)$$

where I_1 and I_3 are the first and the third invariants of the right Cauchy–Green tensor, D_1 and D_2 are the Fung material constants, K_{PEN} is defined as

$$K_{\text{PEN}} = \frac{2D_1 D_2}{(1 - 2\nu_{\text{PEN}})} \quad (10)$$

and ν_{PEN} has a value close to 0.5 [100].

For the Mooney–Rivlin hyperelastic model, the second Piola–Kirchhoff stress tensor is

$$S^{ij} = 2\left(C_1 + C_2 G^{kl} g_{kl}\right) G^{ij} - 2C_2 G^{ik} g_{kl} G^{lj}$$
$$+ \left(K_{\text{PEN}} ln\left(\sqrt{I_3}\right) - 2(C_1 + C_2)\right) g^{ij} \quad (11)$$

where C_1 and C_2 are the Mooney–Rivlin material constants, g^{ij} is the contravariant metric tensor in the deformed configuration and K_{PEN} is defined as [100]

$$K_{\text{PEN}} = \frac{2(C_1 + C_2)}{(1 - 2\nu_{\text{PEN}})} \quad (12)$$

Torii et al. [104] performed FSI simulations using three different models for the arterial wall in cerebral aneurysms: (1) linearly elastic material with small-strain assumption, (2) linearly elastic material with finite strain, and (3) hyperelastic constitutive model. The hyperelastic model was able to reproduce the incompressibility and stiffening behavior of the arterial wall under high strain. Although this model is theoretically more adequate, the linearly elastic models are simpler to implement and the results show that these elastic models can also be useful for the study of the aneurysm-FSI.

3.3.2 FSI. FSIs constitute a multiphysics problem in which one or more solid structures interact with an internal or surrounding fluid flow [105]. Important BCs at the FSI interfaces in hemodynamic studies in cerebral aneurysms are [106,107]:

— displacements of the fluid and solid domains must be compatible: $\boldsymbol{d}_s = \boldsymbol{d}_f$
— tractions at these boundaries must be at equilibrium: $\boldsymbol{\sigma}_s \cdot \hat{n}_s = \boldsymbol{\sigma}_f \cdot \hat{n}_f$
— fluid obeys the no-slip condition: $\boldsymbol{u}_f = \boldsymbol{u}_w$

where d, σ, and $\hat{n}_s$ are the displacement, stress tensor, and unit vector normal to the boundary, with f referring to the fluid and s to the solid [108].

There are essentially two approaches to solve this kind of problem, the monolithic and the partitioned methods. In the former approach, the flow and structural equations are solved simultaneously treating the coupled problem as a whole and allowing for error control, which is favorable for the stability of the calculation. On the other hand, in the partitioned approach each physical field is solved separately, and, therefore, the flow does not change while the solution of the structural equations is calculated and vice versa. This latter approach needs the use of a coupling algorithm to allow for the FSI and to determine the solution of the coupled problem [109,110].

There is another general classification in terms of meshing methodologies: conforming and nonconforming mesh methods. In the first case, the interface conditions are considered as physical BCs, i.e., the interface location is part of the solution, and

continuously defined meshes must conform to the interface and need to accommodate the movement and/or deformation of the solid structure. In the case of nonconforming mesh methods, the fluid and solid equations are solved independently from each other, each within their own grids, with no remeshing necessary [105]. In this case the boundary location and the interface conditions are introduced as constraints. Nonconforming meshing is typically based on immersed methodologies. The immersed boundary method was introduced by Peskin [111] to simulate cardiac mechanics and blood flow, and it is widely used [112,113]. The immersed methods are defined as "a class of FSI methods that add force-equivalent terms to fluid equations to represent the FSI and to avoid mesh update in the numerical procedure. The immersed structure can be either a boundary (e.g., a curve in 2D and a surface in 3D) or a body with finite area (in 2D) or volume (in 3D), either rigid or flexible" [105].

Tezduyar and Sathe [99] and coworkers [100,114–116] developed space–time FSI techniques that have been widely used for years [117], and they recently enhanced this technique, increasing its scope, accuracy, robustness and efficiency by including the deforming-spatial domain/stabilized space–time (DSD/SST) formulation, fluid–structure interface conditions, preconditioning techniques used in iterative solution of the linear equation systems, and a contact algorithm protecting the quality of the fluid mechanics mesh between the structural surfaces that come into contact. These techniques are based on a structural model for arteries developed by that group of authors, and they extended the hyperelastic model to the flow in arteries with aneurysms using patient-specific image based geometries with relative success.

4 Patient-Specific Geometry Models

Although systematic studies with general configurations are insightful to identify trends, imaging techniques required to obtain patient-specific geometric models are becoming increasingly important because of the wide variety of conditions encountered in the human body.

Neal and Kerckhoffs [118] defined patient-specific modeling (PSM) "as the development of computational models of human pathophysiology that are individualized to patient-specific data." As such, patient-specific models have been used in the last decades to obtain very precise geometric models of the brain arteries in order to study the blood dynamics in cerebral aneurysms using CFD [119–121].

The first step for obtaining a virtual model is to acquire patient-specific anatomy. Normally, it relies on the use of noninvasive imaging methods with high-quality to avoid the loss of information from one step to another in image processing [122–124]. Examples of techniques in which these high-quality images are obtained and used to reconstruct the geometric shape of the aneurysms [125] are: ultrasonography, computed tomographic angiography, magnetic resonance (MR) angiography, or rotational cerebral angiography. However, depending on the position of the aneurysm (i.e., basilar artery (BA), posterior communicating arteries (PCoAs) or others), when the blood flow is received from two sources, it is often very difficult to get a complete 3D model to perform patient-specific CFD [126]. Castro et al. [126] developed a method to solve this problem by merging 3D rotational angiography (RA) models from independently acquired rotational angiograms. Once the reconstructed geometry is finalized, the next step involves evaluating the geometry in which the control volume required for CFD simulations is selected.

5 Computational Hemodynamics of Middle Cerebral Aneurysms

Various computational works related with the hemodynamics of middle cerebral saccular aneurysms were carried out in the last decade. These studies were developed with both Newtonian and non-Newtonian fluid models and with different BCs, but there is

Table 4 BCs used in CFD by different authors considering Newtonian models for blood

Reference	Vessel walls	Geometry	Inlet velocity profile	Comments
Castro et al. [127]	Rigid	PSM[a]	Pulsatile (Womersley)	Influence of the upstream parent vessel
Marzo et al. [128]	Nonlinear viscoelastic	PSM	Plug flow and Womersley	Effects of two different inlet transient velocity profiles
Marzo et al. [129]	Rigid	PSM and non-PSM	Flat	Differences between using a patient-specific or modeled BCs
Shojima et al. [130]	Rigid	PSM	Pulsatile (Womersley)	Effect of the WSS
Bazilevs et al. [131]	Rigid and hyperelastic	PSM	Pulsatile	Influence of the FSI in aneurysms rupture
Raschi et al. [132]	Rigid	PSM	Pulsatile (Womersley)	Comparison with in vitro experiments
Cebral et al. [119]	Rigid	PSM	Pulsatile (Womersley)	Evaluation of flow patterns, impingement areas and jet sizes in rupture and unruptured aneurysms
Miura et al. [133]	Rigid	PSM	Pulsatile	Evaluation of the most significant parameters associated with rupture of MCA aneurysms
Omodaka et al. [134]	Rigid	PSM	Flat	Study of the rupture point in relation with local hemodynamics

[a]PSM: patient-specific modeling.

still a lack of studies combining different rheological models for blood flow and wall models describing FSI to predict aneurysm formation, growth, and disruption. In this section, we analyze the results of these contributions as a function of the rheological blood model, aneurysm geometry, BCs, and mechanical behavior of the vessel walls.

5.1 Aneurysm Hemodynamics Using Newtonian Models for Blood. Numerous studies on the hemodynamics of MCA that model blood as an incompressible Newtonian fluid and describe the flow by the unsteady Navier–Stokes equations have been reported. Castro et al. [127] used a blood viscosity of 0.004 Pa·s, assumed rigid vessel walls with no slip BCs and pulsatile inlet velocity profiles using the Womersley solution. The objective was to study the influence of the geometry of the upstream parent vessel on the intraneurysmal hemodynamics. They concluded that the geometry of the upstream parent artery can cause important changes on intraneurysmal hemodynamics, indicating that models without upstream artery geometry may lead to an underestimation of the WSS in the dome and body of the aneurysm. Marzo et al. [128] studied the effects of two different inlet transient velocities on the hemodynamics of intracranial aneurysms: a flat (plug) profile and a spatially developed profile based on Womersley's analytical solution. They considered a blood viscosity of 0.0035 Pa·s and a nonlinear viscoelastic model for the vessel walls, showing initially that there was no change in qualitative flow patterns between the two types of velocity profiles. Subsequently, Marzo et al. [129] used a flat velocity profile and rigid arterial walls to carry out an investigation of modeled hemodynamics using a complete set of BCs from different sources: a 1D model, patient-specific measurements, and other alternatives all quantified via the flow rate and pressure waveforms for inlet and outlet locations. Their results showed significant differences between simulations from patient-specific BCs and from modeled BCs, especially because of differences in the Re of the flow close to the aneurysms.

Shojima et al. [130] modeled blood flow with a viscosity of 0.004 Pa·s in a rigid vessel with a pulsatile flow described by the Womersley velocity profile. They showed that the WSS inside the aneurysm was significantly lower than in the vessel, and that the WSS of the aneurysm was inversely proportional to its AR, which has some connection to the rupture.

Bazilevs et al. [131] proposed a computational framework to accurately simulate the vascular blood flow and FSI of cerebral aneurysms; they considered both rigid and flexible arterial walls

(hyperelastic model) and a pulsatile velocity profile. Their main conclusion was that the interaction between the blood flow and the wall deformation had a large influence on the hemodynamic forces acting on the arterial wall relative to the rigid wall, the use of which was shown to overestimate the wall shear stress magnitude. Moreover, they proved that the WSS depends strongly on the inlet vessel orientation and on the impingement angle of the blood jet on the arterial wall of the aneurysm.

Raschi et al. [132] aimed to describe the hemodynamics during the growth of an aneurysm considering an inlet pulsatile velocity profile according to Womersley. Their computational results compared well with in vitro particle image velocimetry (PIV) experimental data, showing that both approaches were adequate to study the hemodynamics conditions during the growth and rupture of cerebral aneurysms. Cebral et al. [119] used patient-specific 3D rotational angiography images to reconstruct models for CFD in order to characterize the hemodynamics in intracranial aneurysms and its relation with the aneurysm rupture. They considered a pulsatile velocity profile (Womersley) and rigid vessel walls, and found that stable flow patterns, large impingement areas and large jet sizes were better correlated with unruptured aneurysms. In contrast, in the case of ruptured aneurysms there were more disturbed flow patterns, small impingement zones and narrow jets.

More recently, the CFD work of Miura et al. [133] showed that the AR, WSS, normalized WSS, OSI, WSSG, and AFI (defined in Table 1) were important parameters in aneurysm hemodynamics, whereas the size of the aneurysmal dome and the GON were not significantly influencing parameters. Using multivariant analyses they showed that only cases with low WSS were significantly associated with the rupture status of MCA aneurysms, thus concluding that WSS may be the most reliable parameter characterizing the rupture of MCA aneurysms. Omodaka et al. [134] carried out numerical simulations of the hemodynamics at the rupture point of middle cerebral aneurysms using 3D rotational angiography images. They considered a blood viscosity of 0.0035 Pa·s, steady flow velocity and rigid arterial walls, and the results showed that low WSS is related with the rupture point at the aneurysm wall.

All these results, which are summarized in Table 4, highlight the necessity of designing appropriate geometries that match as much as possible the real features of the vessel, with patient-specific BCs, instead of modeled BCs, and defining a consistent interaction between the blood flow and the wall deformation. All these aspects have been shown to alter the hemodynamics, and their omission leads to an overestimation of the WSS in the aneurysms.

Table 5 BCs used in CFD by different authors considering non-Newtonian models for blood

Reference	Vessel walls	Geometry	Inlet velocity profile	Comments
Wang et al. [138]	Rigid	PSM[a]	Pulsatile (Womersley)	Correlation between the growth and rupture of the daughter saccule and the hemodynamics
Bernabeu et al. [139]	Rigid	PSM	Pulsatile (Womersley)	Effects of the rheological model for blood on the WSS
Valencia et al. [137]	Rigid	PSM	Pulsatile (Womersley)	Effects of the non-Newtonian properties of blood in hemodynamic factors and WSS
Valencia et al. [140]	Rigid	Non-PSM	Pulsatile (Womersley)	Effects of aneurysm geometry and non-Newtonian properties on flow characteristics, wall pressure and WSS
Evju et al. [141]	Rigid	PSM	Pulsatile (Womersley)	Effects of different viscosity models, different inflow conditions and different out flow conditions

[a]PSM: patient-specific modeling.

5.2 Aneurysm Hemodynamics Using Non-Newtonian Models for Blood. It has been reported that the non-Newtonian properties of blood inside cerebral aneurysms affect the flow characteristics in a non-negligible way, especially when the flow rate through the vessel is low [135–137]. Valencia et al. [58] reported that the differences between the Newtonian and non-Newtonian fluid models have a significant impact on the WSS only when the flow dynamics are unsteady. Notwithstanding the importance of the complex behavior of blood flow, very few other studies related with the numerical simulation of hemodynamics in middle cerebral aneurysms were carried out using non-Newtonian models for blood.

Wang et al. [138] and Bernabeu et al. [139] used CFD to study the hemodynamics in middle cerebral aneurysms assuming blood as a Generalized-Newtonian fluid with the blood viscosity described by the Carreau–Yasuda (C-Y) model, together with rigid arterial walls and pulsatile inlet velocity profiles according to Womersley. Wang et al. [138] studied the hemodynamic factors in a patient-specific geometry with daughter saccules obtained from cerebral angiography with 180 deg rotational scanning. They used WSS or OSI with the aim of finding a correlation between the growth and rupture of the daughter saccule and the hemodynamics. They concluded that a high OSI (close to 0.5) is responsible for a complex unstable flow and can cause the growth of the daughter saccules. Bernabeu et al. [139] worked with a patient-specific 3D model of a middle cerebral aneurysm in order to compare the effect of the rheological model for blood on the WSS. They reported that a WSS signal with a strong oscillatory component indicates aneurysm rupture risk for thresholds greater than or equal to 1.56 Pa in the Newtonian case, and 0.94 Pa in the case of the C-Y model. However, with nonoscillatory WSS, the results obtained were identical for both models.

The Herschel–Bulkley yield stress model was also used by some authors to study the hemodynamics in MCA [58,137,140]. Valencia et al. [137] developed numerical simulations of 3D unsteady flow using patient-specific models from 3D rotational angiography images, pulsatile flow following the Womersley solution and rigid walls. Their aim was to study the effects of the non-Newtonian characteristic of blood on the hemodynamic factors and on the WSS. They showed that the predictions of velocity, pressure and WSS distributions obtained with Newtonian and non-Newtonian models present significant differences only in regions with high velocity, especially in the case of unsteady flow. They also explained that low values of WSS could be closely related with a deterioration of the arterial walls. Similar BCs were used in another work of Valencia et al. [140] to evaluate the effects of the aneurysm geometry and non-Newtonian blood flow in the hemodynamics, wall pressure, and wall shear stress. More recently, Evju et al. [141] studied the influence of using different viscosity models (Newtonian, a modified Cross and Casson models), in combination with different inflow and outflow BCs, upon the flow characteristic in MCA aneurysms considering rigid vessel walls. They found significant impact on some parameters such as

the maximum and the average WSS of the aneurysm sac (MWSS and AWSS, respectively) and the area of low shear given as a percentage of the total sac area [141]. Although they found some correlations between these quantities and those viscosity models and BCs, there is no strong correspondence between the WSS parameters and the type, size, or shape of the aneurysms. A summary of these results can be found in Table 5.

Most of the works comparing the influence of Newtonian and non-Newtonian blood models upon the hemodynamics of MCA concluded that different flow patterns are obtained, with the Newtonian model usually leading to an underestimation of the principal hemodynamic factors. However, no studies dealing with the hemodynamics in MCA have been carried out with viscoelastic models for blood. It is clear that an accurate description of MCA requires the use of non-Newtonian blood models in general and, perhaps, viscoelastic models in particular since these models take into account the elasticity and other structural aspects of the blood, which could lead to a better insight the initiation, growth, and rupture of aneurysms. It is important to highlight that very recently, Dimakopoulos et al. [142] performed numerical simulations of the hemodynamics in stenotic microvessels using the non-homogeneous viscoelastic model proposed by Moyers-Gonzalez et al. [21], concluding that only the viscoelastic model of blood was able to reproduce the experimental observations. A similar impact is expected in hemodynamics of MCA, and therefore further numerical simulations using the non-Newtonian models shown in Tables 2 and 3 are required in order to fully understand the hemodynamics of MCA.

Nevertheless, it is also worth pointing out that some works considering a Newtonian behavior for blood, showed a large variability in reported results obtained using different flow solver packages [143], which owes more to the different solution strategies and discretization methods used than to the choice of the outlet or inlet BCs or of the software itself [144].

6 Final Remarks and Future Directions

Many published studies investigating the hemodynamics in middle cerebral aneurysms consider Newtonian blood models, rigid or nonrigid walls and steady flow conditions. Such conditions produce results that differ significantly from those carried out using FSI between the blood flow and the vessel wall, time-dependent flow conditions, and non-Newtonian models for blood flow.

Computational hemodynamics using Newtonian models, and/or simplified geometries are good approximations to obtain first-hand qualitative results. They allow establishing qualitative trends identifying the possible roles of mechanisms of aneurysm initiation and growth, but are not adequate for a more quantitative analysis. The studies of hemodynamics in cerebral aneurysms following a patient-specific approach, combining medical imaging, CFD analysis, and knowledge of biological responses to hemodynamics forces, can provide a good insight into this

pathology. However, quantitative validation of image-based CFD analysis against experimental and in vivo data has, to date, not been fully addressed. In fact, CFD is still far from being a tool used directly in the clinical context of cardiovascular diseases. To move a step forward in this direction, a number of important considerations need to be taken into account in the future, as summarized below.

— The rheological model for blood should be as accurate as possible. In particular, when dealing with time-dependent flow in small vessels, a viscoelastic model (non-Newtonian) able to predict shear-thinning behavior, memory effects, and normal-stress effects should be used. Ideally, these models should also reflect the specific mechanisms that affect those rheological properties such as formation/disruption of rouleaux.
— Patient-specific models able to reproduce the correct aneurysm/vessel geometry as well as adequate inlet velocity profile, and inlet and outlet pressure conditions.
— Realistic arterial wall deformation models that are able to reflect its mechanical behavior.
— The biochemical response of the vessel walls to the mechanical request and the way it affects the wall constitutive equation.

These considerations would lead to a more realistic assessment of the blood flow dynamics and would increase the potential of this powerful tool in the diagnostic and guidance of medical treatment of cardiovascular diseases.

Recently, multiscale approaches that couple different models operating at different space scales involving local and systemic dynamics [145] have become more common for the study of the human cardiovascular system. For instance, Forsyth et al. [146] used a multiscale approach to understand the links between single RBC dynamics, ATP release and macroscopic viscosity, all at physiological shear rates. Xu et al. [147] developed a multiscale model to study clot formation under various flow conditions; and Grinberg et al. [148] proposed a multiscale approach for modeling arterial blood flow including modeling of the initial thrombus formation. The multiscale approach combines the relative simplicity and efficiency of CFD macroscopic models with the accuracy of microscopic models, and has the potential to shed new light into the macro–micro relationships involving the blood plasma, RBCs, platelets, and/or RBC aggregates. Despite its large computational cost, multiscale approaches are likely to lead to exciting developments in computational modeling of hemodynamic flow in aneurysms.

Acknowledgment

References

[1] Deaton, C., Froelicher, E. S., Wu, L. H., Ho, C., Shishani, K., and Jaarsma, T., 2011, "The Global Burden of Cardiovascular Disease," J. Cardiovasc. Nurs., 26, pp. S5–S14.

[2] Zarins, C. K., Giddens, D. P., Bharadvaj, B. K., Sottiurai, V. S., Mabon, R. F., and Glagov, S., 1983, "Carotid Bifurcation Atherosclerosis: Quantitative Correlation of Plaque Localization With Flow Velocity Profiles and Wall Shear Stress," Circ. Res., 53(4), pp. 502–514.

[3] Thubrikar, M. J., Al-Soudi, J., and Robicsek, F., 2001, "Wall Stress Studies of Abdominal Aortic Aneurysm in a Clinical Model," Ann. Vasc. Surg., 15(3), pp. 355–366.

[4] Ujiie, H., Tamano, Y., Sasaki, K., and Hori, T., 2001, "Is the Aspect Ratio a Reliable Index for Predicting the Rupture of a Saccular Aneurysm?," Neurosurgery, 48(3), pp. 495–502.

[5] Szikora, I., Páal, G., and Ugron, A., 2008, "Impact of Aneurysmal Geometry on Intraaneurysmal Flow: A Computerized Flow Simulation Study," Neuroradiology, 50(5), pp. 411–421.

[6] Imbesi, S. G., and Kerber, C. W., 1999, "Analysis of Slipstream Flow in Two Tuptured Intracranial Cerebral Aneurysms," Am. J. Neuroradiol., 20(9), pp. 1703–1705.

[7] Moyers-Gonzalez, M., Owens, R. G., and Fang, J., 2008, "A Non-Homogeneous Constitutive Model for Human Blood. Part III. Oscillatory Flow," J. Non-Newtonian Fluid Mech., 155(3), pp. 161–173.

[8] Eckmann, D. M., Bowers, S., Stecker, M., and Cheung, A. T., 2000, "Hematocrit, Volume Expander, Temperature, and Shear Rate Effects on Blood Viscosity," Anesth. Analg., 91(3), pp. 539–545.

[9] Merrill, E. W., 1969, "Rheology of Blood," Physiol. Rev., 49, pp. 863–888.

[10] Thurston, G. B., 1979, "Rheological Parameters for the Viscosity, Viscoelasticity and Thixotropy of Blood," Biorheology, 16, pp. 149–162.

[11] Dintenfass, L., 1963, "Blood Rheology in Cardio-Vascular Diseases," Nature, 199, pp. 813–815.

[12] Langstroth, L., 1919, "Blood Viscosity. I Conditions Affecting the Viscosity of Blood After Withdrawal From the Body," J. Exp. Med., 30(6), pp. 597–606.

[13] Chien, S., Usami, S., Dellenback, R. J., and Gregersen, M. I., 1967, "Blood Viscosity: Influence of Erythrocyte Deformation," Science, 157(3790), pp. 827–829.

[14] Chien, S., Usami, S., Dellenback, R. J., Gregersen, M. I., Nanninga, L. B., and Guest, M. M., 1967, "Blood Viscosity: Influence of Erythrocyte Aggregation," Science, 157(3790), pp. 829–831.

[15] Morrison, F. A., 2001, Understanding Rheology, Oxford University, Inc., New York.

[16] Campo-Deaño, L., Dullens, R. P. A., Aarts, D. G. L. A., Pinho, F. T., and Oliveira, M. S. N., 2013, "Viscoelasticity of Blood and Viscoelastic Blood Analogues for Use in Polydimethylsiloxane in Vitro Models of the Circulatory System," Biomicrofluidics, 7(3), p. 034102.

[17] Poole, R. J., 2012, "The Deborah and Weissenberg Numbers," British Soc. Rheol. Rheol. Bull., 53, pp. 32–39.

[18] Galindo-Rosales, F. J., Campo-Deaño, L., Sousa, P. C., Ribeiro, V. M., Oliveira, M. S. N., Alves, M. A., and Pinho, F. T., 2014, "Viscoelastic Instabilities in Micro-Scale Flows," Experimental Thermal and Fluid Science, 59, pp. 128–129.

[19] Gijsen, F. J. H., van de Vosse, F. N., and Janssen, J. D., 1999, "The Influence of the Non-Newtonian Properties of Blood on the Flow in Large Arteries: Steady Flow in a Carotid Bifurcation Model," J. Biomech., 32(6), pp. 601–608.

[20] Owens, R. G., 2006, "A New Microstructure-Based Constitutive Model for Human Blood," J. Non-Newtonian Fluid Mech., 140(1–3), pp. 57–70.

[21] Moyers-Gonzalez, M., Owens, R. G., and Fang, J., 2008, "A Non-Homogeneous Constitutive Model for Human Blood. Part I. Model Derivation and Steady Flow," J. Fluid Mech., 617, pp. 327–354.

[22] Moyers-Gonzalez, M., and Owens, R. G., 2008, "A Non-Homogeneous Constitutive Model for Human Blood. Part II. Asymptotic Solution for Large Péclet Numbers," J. Non-Newtonian Fluid Mech., 155(3), pp. 146–160.

[23] Sforza, D. M., Putman, C. M., and Cebral, J. R., 2012, "Computational Fluid Dynamics in Brain Aneurysms," Int. J. Numer. Methods Biomed. Eng., 28(6–7), pp. 801–808.

[24] Markwalder, T. M., Grolimund, P., Seiler, R. W., Roth, F., and Aaslid, R., 1984, "Dependency of Blood Flow Velocity in the Middle Cerebral Artery on End-Tidal Carbon Dioxide Partial Pressure- A Transcranial Ultrasound Doppler Study," J. Cereb. Blood Flow Metab., 4(3), pp. 368–372.

[25] Vlachos, N. S., and Whitelaw, J. H., 1974, "The Measurement of Blood Velocity With Laser Anemometry," Proceedings, Volume 1, No. A76-10426 01-35, Purdue University, West Lafayette, IN, pp. 521–540., In: International Workshop on Laser Velocimetry, 2nd, West Lafayette, Ind., March 27–29, 1974.

[26] Lasheras, J. C., 2007, "The Biomechanics of Arterial Aneurysms," Annu. Rev. Fluid Mech., 39(1), pp. 293–319.

[27] Sforza, D. M., Putman, C. M., and Cebral, J. R., 2009, "Hemodynamics of Cerebral Aneurysms," Annu. Rev. Fluid Mech., 41, pp. 91–107.

[28] Withers, K., Carolan-Rees, G., and Dale, M., 2013, "Pipeline™ Embolization Device for the Treatment of Complex Intracranial Aneurysms. A NICE Medical Technology Guidance," Appl. Health Econ. Health Policy, 11, pp. 5–13.

[29] Foutrakis, G. N., Yonas, H., and Sclabassi, R. J., 1999, "Saccular Aneurysm Formation in Curved and Bifurcating Arteries," Am. J. Neuroradiol., 20(7), pp. 1309–1317.

[30] Massoud, T. F., Turjman, F., Ji, C., Viñuela, F., Guglielmi, G., Gobin, Y. P., and Duckwiler, G. R., 1995, "Endovascular Treatment of Fusiform Aneurysms With Stents and Coils: Technical Feasibility in a Swine Model," Am. J. Neuroradiol., 16(10), pp. 1953–1963.

[31] Raghavan, M. L., Ma, B., and Harbaugh, R. E., 2005, "Quantified Aneurysm Shape and Rupture Risk," J. Neurosurg., 102(2), pp. 355–362.

[32] Parlea, L., Fahrig, R., Holdsworth, D. W., and Lownie, S. P., 1999, "An Analysis of the Geometry of Saccular Intracranial Aneurysms," Am. J. Neuroradiol., 20(6), pp. 1079–1089.

[33] Ma, B., Harbaugh, R. B., and Raghavan, M. L., 2004, "Three-Dimensional Geometrical Characterization of Cerebral Aneurysms," Ann. Biomed. Eng., 32(2), pp. 264–273.

[34] Lauric, A., Miller, E. L., Baharoglu, M. I., and Malek, A. M., 2011, "3D Shape Analysis of Intracranial Aneurysms Using the Writhe Number as a Discriminant for Rupture," Ann. Biomed. Eng., 39(5), pp. 1457–1469.

[35] Hoh, B. L., Sistrom, C. L., Firment, C. S., Fautheree, G. L., Velat, G. J., Whiting, J. H., Reavey-Cantwell, J. F., and Lewis, S. B., 2007, "Bottleneck Factor and Height-Width Ratio: Association With Ruptured Aneurysms in Patients With Multiple Cerebral Aneurysms," Neurosurgery, **61**(4), pp. 716–723.

[36] Ujiie, H., Tachibana, H., Hiramatsu, O., Hazel, A. L., Matsumoto, T., Ogasawara, Y., Nakajima, H., Hori, T., Takakura, K., and Kajiya, F., 1999, "Effects of Size and Shape (Aspect Ratio) on the Hemodynamics of Saccular Aneurysms: A Possible Index for Surgical Treatment of Intracranial Aneurysms," Neurosurgery, **45**(1), pp. 119–130.

[37] Fuller, F. B., 1971, "The Writhing Number of a Space Curve," Proc. Natl. Acad. Sci. U.S.A., **68**(4), pp. 815–819.

[38] Tremmel, M., Dhar, S., Levy, E., Mocco, J., and Meng, H., 2009, "Influence of Intracranial Aneurysms-to-Parent Vessel Size Ratio on Hemodynamics and Implication for Rupture: Results From a Virtual Experimental Study," Neurosurgery, **64**(4), pp. 622–631.

[39] Ku, D. N., Giddens, D. P., Zarins, C. K., and Glagov, S., 1985, "Pulsatile Flow and Atherosclerosis in the Human Carotid Bifurcation. Positive Correlation Between Plaque Location and Low and Oscillating Shear Stress," Arterioscler., Thromb., Vasc. Biol., **5**(3), pp. 293–302.

[40] Mantha, A., Karmonik, C., Benndorf, G., Strother, C., and Metcalfe, R., 2006, "Hemodynamics in a Cerebral Artery Before and After the Formation of an Aneurysm," Am. J. Neuroradiol., **27**(5), pp. 1113–1118.

[41] Shimogonya, Y., Ishikawa, T., Imai, Y., Matsuki, N., and Yamaguchi, T., 2009, "Can Temporal Fluctuation in Spatial Wall Shear Stress Gradient Initiate a Cerebral Aneurysm? A Proposed Novel Hemodynamic Index, the Gradient Oscillatory Number (GON)," J. Biomech., **42**(4), pp. 550–554.

[42] Jou, L.-D., and Mawad, M. E., 2011, "Timing and Size of Flow Impingement in a Giant Intracranial Aneurysm at the Internal Carotid Artery," Med. Biol. Eng. Comput., **49**(8), pp. 891–899.

[43] Zuleger, D. I., Poulikakos, D., Valavanis, A., and Kollias, S. S., 2010, "Combining Magnetic Resonance Measurements With Numerical Simulations – Extracting Blood Flow Physiology Information Relevant to the Investigation of Intracranial Aneurysms in the Circle of Willis," Int. J. Heat Fluid Flow, **31**(6), pp. 1032–1039.

[44] Kojima, M., Irie, K., Keda, S., Fukuda, T., Arai, F., Hirose, Y., and Negoro, M., 2012, "The Hemodynamic Study for Growth Factor Evaluation of Rupture Cerebral Aneurysm Followed up for Five Years," J. Biomed. Sci. Eng., **5**(12A), pp. 884–891.

[45] Irie, K., Anzai, H., Kojima, M., Honjo, N., Ohta, M., Hirose, Y., and Negoro, M., 2012, "Computational Fluid Dynamic Analysis Following Recurrence of Cerebral Aneurysm After Coil Embolization," Asian J. Neurosurg., **7**(3), pp. 109–115.

[46] Sforza, D. M., Putman, C. M., Tateshima, S., Viñuela, F., and Cebral, J. R., 2012, "Effects of Perianeurysmal Environment During the Growth of Cerebral Aneurysms: A Case Study," Am. J. Neuroradiol., **33**(6), pp. 1115–1120.

[47] Tanoue, T., Tateshima, S., Villablanca, J. P., Viñuela, F., and Tanishita, K., 2011, "Wall Shear Stress Distribution Inside Growing Cerebral Aneurysm," Am. J. Neuroradiol., **32**(9), pp. 1732–1737.

[48] Boussel, L., Rayz, V., McCulloch, C., Martin, A., Acevedo-Bolton, G., Lawton, M., Higashida, R., Smith, W. S., Young, W. L., and Saloner, D., 2008, "Aneurysm Growth Occurs at Region of Low Wall Shear Stress: Patient-Specific Correlation of Hemodynamics and Growth in a Longitudinal Study," Stroke, **39**(11), pp. 2997–3002.

[49] Jou, L.-D., Wong, G., Dispensa, B., Lawton, M. T., Higashida, R. T., Young, W. L., and Saloner, D., 2005, "Correlation Between Lumenal Geometry Changes and Hemodynamics in Fusiform Intracranial Aneurysms," Am. J. Neuroradiol., **26**(9), pp. 2357–2363.

[50] Rayz, V. L., Boussel, L., Ge, L., Leach, J. R., Martin, A. J., Lawton, M. T., McCulloch, C., and Saloner, D., 2010, "Flow Residence Time and Regions of Intraluminal Thrombus Deposition in Intracranial Aneurysms," Ann. Biomed. Eng., **38**(10), pp. 3058–3069.

[51] Valant, A. Z., Ziberna, L., Papaharilaou, Y., Anayiotos, A., and Georgiou, G. C., 2011, "The Influence of Temperature on Rheological Properties of Blood Mixtures With Different Volume Expanders—Implications in Numerical Arterial Hemodynamics Simulations," Rheol. Acta, **50**(4), pp. 389–402.

[52] Caro, C. G., Pedley, T. J., Schroter, R. C., and Seed, W. A., 2012, The Mechanics of the Circulation, Cambridge University, New York.

[53] Vlastos, G., Lerche, D., Koch, B., Samba, O., and Pohl, M., 1997, "The Effect of Parallel Combined Steady and Oscillatory Shear Flows on Blood and Polymer Solutions," Rheol. Acta, **36**(2), pp. 160–172.

[54] Sousa, P. C., Carneiro, J., Vaz, R., Cerejo, A., Pinho, F. T., Alves, M. A., and Oliveira, M. S. N., 2013, "Shear Viscosity and Nonlinear Behavior of Whole Blood Under Large Amplitude Oscillatory Shear," Biorheology, **50**(5–6), pp. 269–282.

[55] Boyd, J., Buick, J. M., and Green, S., 2007, "Analysis of the Casson and Carreau-Yasuda Non-Newtonian Blood Models in Steady and Oscillatory Flows Using the Lattice Boltzmann Method," Phys. Fluids, **19**(9), p. 093103.

[56] Razavi, A., Shirani, E., and Sadeghi, M. R., 2011, "Numerical Simulation of Blood Pulsatile Flow in a Stenosed Carotid Artery Using Different Rheological Models," J. Biomech., **44**(11), pp. 2021–2030.

[57] Molla, M. M., and Paul, M. C., 2012, "LES of Non-Newtonian Physiological Blood Flow in a Model of Arterial Stenosis," Med. Eng. Phys., **34**(8), pp. 1079–1087.

[58] Valencia, A., Morales, H., Rivera, R., Bravo, E., and Galvez, M., 2008, "Blood Flow Dynamics in Patient-Specific Cerebral Aneurysm Models: The Relationship Between Wall Shear Stress and Aneurysm Area Index," Med. Eng. Phys., **30**(3), pp. 329–340.

[59] Amornsamankul, S., Wiwatanapataphee, B., Wu, Y. H., and Lenbury, Y., 2005, "Effect of Non-Newtonian Behavior of Blood on Pulsatile Flows in Stenotic Arteries," Int. J. Biol. Life Sci., **1**, pp. 42–46.

[60] Anand, M., and Rajagopal, K. R., 2004, "A Shear-Thinning Viscoelastic Fluid Model for Describing the Flow of Blood," Int. J. Cardiovasc. Med. Sci., **4**, pp. 59–68.

[61] Robertson, A. M., Sequeira, A., and Owens, R. G., 2009, "Rheological Models for Blood," Cardiovascular Mathematics: Modeling and Simulation of the Circulatory System, L. Formaggia, A. Quarteroni, A. Veneziani, eds., Springer-Verlag, Milano, Italy.

[62] Bodnár, T., Sequeira, A., and Pirkl, L., 2009, "Numerical Simulations of Blood Flow in a Stenosed Vessel Under Different Flow Rates Using a Generalized Oldroyd-B Model," International Conference on Numerical Analysis and Applied Mathematics, Rethymno, Crete, Sept. 18–22, Vol. 2, pp. 645–648.

[63] Yilmaz, F., and Gundogdu, M. Y., 2008, "A Critical Review on Blood Flow in Large Arteries; Relevance to Blood Rheology, Viscosity Models, and Physiologic Conditions," Korea-Australia Rheol. J., **20**, pp. 197–211.

[64] Stuart, J., and Kenny, M. W., 1980, "Blood Rheology," J. Clin. Pathol., **33**(5), pp. 417–429.

[65] Antonova, N., 2012, "On Some Mathematical Models in Hemorheology," Biotechnol. Biotechnol. Equip., **26**(5), pp. 3286–3291.

[66] Giesekus, H., 1982, "A Simple Constitutive Equation for Polymer Fluids Based on the Concept of Deformation-Dependent Tensorial Mobility," J. Non-Newtonain Fluid Mech., **11**(1–2), pp. 69–109.

[67] Phan-Thien, N., and Tanner, R. I., 1977, "A New Constitutive Equation Derived From Network Theory," J. Non-Newtonain Fluid Mech., **2**(4), pp. 353–365.

[68] Bureau, M., Healy, J. C., Bourgoin, D., and Joly, M., 1980, "Rheological Hysteresis of Blood at Low Shear Rate," Biorheology, **17**(1–2), pp. 191–203.

[69] Oldroyd, J. G., 1950, "On the Formulation of Rheological Equation of State," Proc. R. Soc. London, Ser. A., **200**(1063), pp. 523–541.

[70] Javadzadegan, J., Esmaeili, M., Majidi, S., and Fakhimghanbarzadeh, B., 2009, "Pulsatile Flow of Viscous and Viscoelastic Fluids in Constricted Tubes," J. Mech. Sci. Technol., **23**(9), pp. 2456–2467.

[71] Yeleswarapu, K. K., Kameneva, M. V., Rajagopal, K. R., and Antaki, J. F., 1998, "The Flow of Blood in Tubes: Theory and Experiment," Mech. Res. Commun., **25**(3), pp. 257–262.

[72] Ku, D. N., 1997, "Blood Flow in Arteries," Annu. Rev. Fluid Mech., **29**(1), pp. 399–434.

[73] Elad, D., and Einav, S., 2004, "Physical and Flow Properties of Blood. Source," Standard Handbook of Biomedical Engineering and Design, pp. 1–25.

[74] Xiao, N., Humphrey, J. D., and Figueroa, C. A., 2013, "Multi-Scale Computational Model of Three-Dimensional Hemodynamics Within a Deformable Full-Body Arterial Network," J. Comput. Phys., **244**, pp. 22–40.

[75] Smith, N. P., Pullan, A. J., and Hunter, P. J., 2002, "An Anatomically Based Model of Transient Coronary Blood Flow in the Heart," SIAM J. Appl. Math., **62**(3), pp. 990–1018.

[76] Womersley, J. R., 1955, "Method for the Calculation of Velocity, Rate of Flow and Viscous Drag in Arteries When the Pressure Gradient is Known," J. Physiol., **127**(2), pp. 553–563.

[77] Fung, Y., 1996, Biomechanics Circulation, Springer, Berlin, Germany.

[78] Banerjee, M. K., Ganguly, R., and Datta, A., 2012, "Effect of Pulsatile Flow Waveform and Womersley Number on the Flow in Stenosed Arterial Geometry," ISRN Biomath., **2012**, p. 853056.

[79] Campbell, I. C., Ries, J., Dhawan, S. S., Quyyumi, A. A., Taylor, W. R., and Oshinski, J. N., 2012, "Effect of Inlet Velocity Profiles on Patient-Specific Computational Fluid Dynamics Simulations of the Carotid Bifurcation," ASME J. Biomech. Eng., **134**(5), p. 051001.

[80] Grinberg, L., and Karniadakis, G., 2008, "Outflow Boundary Conditions for Arterial Networks With Multiple Outlets," Ann. Biomed. Eng., **36**(9), pp. 1496–1514.

[81] Ramalho, S., Moura, A., Gambaruto, A. M., and Sequeira, A., 2012, "Sensitivity to Outflow Boundary Conditions and Level of Geometry Description for a Cerebral Aneurysm," Int. J. Numer. Methods Biomed. Eng., **28**(6–7), pp. 697–713.

[82] Papanastasiou, T. C., Malamataris, N., and Ellwood, K., 1992, "A New Outflow Boundary Condition," Int. J. Numer. Methods Fluids, **14**(5), pp. 587–608.

[83] Malamataris, N. T., and Papanastasiou, T. C., 1991, "Unsteady Free Surface Flows on Truncated Domains," Ind. Eng. Chem. Res., **30**(9), pp. 2211–2219.

[84] Griffiths, D. F., 1997, "The 'No Boundary Condition' Outflow Boundary Condition," Int. J. Numer. Methods Fluids, **24**(4), pp. 393–411.

[85] Renardy, M., 1997, "Imposing No Boundary Condition at Outflow: Why Does It Work?," Int. J. Numer. Methods Fluids, **24**(4), pp. 413–417.

[86] Park, S. J., and Lee, S. J., 1999, "On the Use of the Open Boundary Condition Method in the Numerical Simulation of Nonisothermal Viscoelastic Flow," J. Non-Newtonian Fluid Mech., **87**(2–3), pp. 197–214.

[87] Moon, J. Y., Suh, D. C., Lee, Y. S., Kim, Y. W., and Lee, J. S., 2014, "Considerations of Blood Properties, Outlet Boundary Conditions and Energy

Loss Approaches in Computational Fluid Dynamics Modeling," Neurointervention, **9**(1), pp. 1–8.

[88] Vignon-Clementel, I. E., Figueroa, C. A., Jansen, K. E., and Taylor, C. A., 2006, "Outflow Boundary Conditions for Three-Dimensional Finite Element Modeling of Blood Flow and Pressure in Arteries," Comput. Methods Appl. Mech. Eng., **195**(29–32), pp. 3776–3796.

[89] Vignon, I. E., and Taylor, C. A., 2004, "Outflow Boundary Conditions for One-Dimensional Finite Element Modeling of Blood Flow and Pressure Waves in Arteries," Wave Motion, **39**(4), pp. 361–374.

[90] Figueroa, C. A., Vignon-Clementel, I. E., Jansen, K. E., Hughes, T. J. R., and Taylor, C. A., 2006, "A Coupled Momentum Method for Modeling Blood Flow in Three-Dimensional Deformable Arteries," Comput. Methods Appl. Mech. Eng., **195**(41–43), pp. 5685–5706.

[91] Westerhof, N., Bosman, F., DeVries, C. J., and Noordergraaf, A., 1969, "Analogue Studies of the Human Systemic Arterial Tree," J. Biomech., **2**(2), pp. 121–143.

[92] Olufsen, M. S., and Nadim, A., 2004, "On Deriving Lumped Models for Blood Flow and Pressure in the Systemic Arteries," Math. Biosci. Eng., **1**(1), pp. 61–80.

[93] Vignon-Clementel, I. E., Figueroa, C. A., Jansen, K. E., and Taylor, C. A., 2010, "Outflow Boundary Conditions for 3D Simulations of Non-Periodic Blood Flow and Pressure Fields in Deformable Arteries," Comput. Methods Biomech. Biomed. Eng., **13**(5), pp. 625–640.

[94] Esmaily-Moghadam, M., Vignon-Clementel, I. E., Figliola, R., and Marsden, A. L., f. t. M. O. C. H. A. M. I., 2013, "A Modular Numerical Method for Implicit 0D/3D Coupling in Cardiovascular Finite Element Simulations," J. Comput. Phys., **244**, pp. 63–79.

[95] O'Rourke, M. F., Staessen, J. A., Vlachopoulos, C., Duprez, D., and Plante, G. E., 2002, "Clinical Applications of Arterial Stiffness; Definitions and Reference Values," Am. J. Hypertens., **15**(5), pp. 426–444.

[96] Couade, M., Pernot, M., Prada, C., Messas, E., Emmerich, J., Bruneval, P., Criton, A., Fink, M., and Tanter, M., 2010, "Quantitative Assessment of Arterial Wall Biomechanical Properties Using Shear Wave Imaging," Ultrasound Med. Biol., **36**(10), pp. 1662–1676.

[97] Deng, S. X., Tomioka, J., Debes, J. C., and Fung, Y. C., 1994, "New Experiments on Shear Modulus of Elasticity of Arteries," Am. J. Physiol. Heart Circ. Physiol., **266**(1 Pt 2), pp. H1–H10.

[98] Balzani, D., Brinkhues, S., and Holzapfel, G. A., 2012, "Constitutive Framework for the Modeling of Damage in Collagenous Soft Tissues With Application to Arterial Walls," Comput. Methods Appl. Mech. Eng., **213–216**, pp. 139–151.

[99] Tezduyar, T. E., and Sathe, S., 2007, "Modeling of Fluid-Structure Interactions With Space-Time Finite Elements: Solution Techniques," Int. J. Numer. Methods Fluids, **54**(6–8), pp. 855–900.

[100] Tezduyar, T. E., Sathe, S., Schwaab, M., and Conklin, B. S., 2008, "Arterial Fluid Mechanics Modeling With the Stabilized Space-Time Fluid-Structure Interaction Technique," Int. J. Numer. Methods Fluids, **57**(5), pp. 601–629.

[101] Fung, Y., 1993, *Biomechanics: Mechanical Properties of Living Tissues*, 2nd ed., Springer, Berlin.

[102] Mooney, M., 1940, "A Theory of Large Elastic Deformation," J. Appl. Phys., **11**(9), pp. 582–592.

[103] Rivlin, R. S., 1948, "Large Elastic Deformations of Isotropic Materials. IV. Further Developments of the General Theory," Philos. Trans. R. Soc. London, Ser. A, **241**(835), pp. 379–397.

[104] Torii, R., Oshima, M., Kobayashi, T., Takagi, K., and Tezduyar, T. E., 2008, "Fluid-Structure Interaction Modeling of a Patient-Specific Cerebral Aneurysm: Influence of Structural Modeling," Comput. Mech., **43**(1), pp. 151–159.

[105] Hou, G., Wang, J., and Layton, A., 2012, "Numerical Methods for Fluid-Structure Interaction—A Review," Commun. Comput. Phys., **12**(2), pp. 337–377.

[106] Valencia, A., Burdiles, P., Ignat, M., Mura, J., Bravo, E., Rivera, R., and Sordo, J., 2013, "Fluid Structural Analysis of Human Cerebral Aneurysm Using Their Own Wall Mechanical Properties," Comput. Math. Method Med., **2013**(5), p. 293128.

[107] Lee, C. J., Zhang, Y., Takao, H., Murayama, Y., and Qian, Y., 2013, "A Fluid-Structure Interaction Study Using Patient-Specific Ruptured and Unruptured Aneurysm: The Effect of Aneurysm Morphology, Hypertension and Elasticity," J. Biomech., **46**(14), pp. 2402–2410.

[108] Valencia, A., and Solis, F., 2006, "Blood Flow Dynamics and Arterial Wall Interaction in a Saccular Aneurysm Model of the Basilar Artery," Comput. Struct., **84**(21), pp. 1326–1337.

[109] Degroote, J., Bathe, K.-J., and Vierendeels, J., 2009, "Performance of a New Partitioned Procedure Versus a Monolithic Procedure in Fluid-Structure Interaction," Comput. Struct., **87**(11–12), pp. 793–801.

[110] Young, Y. L., Chae, E. J., and Akcabay, D. T., 2012, "Hybrid Algorithm for Modeling of Fluid-Structure Interaction in Incompressible, Viscous Flows," Acta Mech. Sin., **28**(4), pp. 1030–1041.

[111] Peskin, C. S., 2002, "The Immersed Boundary Method," Acta Numer., **11**, pp. 479–517.

[112] Jendoubi, A., Yakoubi, D., Fortin, A., and Tibirna, C., 2014, "An Immersed Boundary Method for Fluid Flows Around Rigid Objects," Int. J. Numer. Methods Fluids, **75**(1), pp. 63–80.

[113] Mittal, R., and Iaccarino, G., 2005, "Immersed Boundary Methods," Annu. Rev. Fluid Mech., **37**(1), pp. 239–261.

[114] Tezduyar, T. E., Sathe, S., Cragin, T., Nanna, B., Conklin, B. S., Pausewang, J., and Schwaab, M., 2007, "Modeling of Fluid-Structure Interactions With Space-Time Finite Elements: Arterial Fluid Mechanics," Int. J. Numer. Methpds Fluids, **54**(6–8), pp. 901–922.

[115] Takizawa, K., Moorman, C., Wright, S., Purdue, J., Mcphail, T., Chen, P. R., Warren, J., and Tezduyar, T. E., 2011, "Patient-Specific Arterial Fluid-Structure Interaction Modeling of Cerebral Aneurysms," Int. J. Numer. Methods Fluids, **65**(1–3), pp. 308–323.

[116] Tezduyar, T. E., T. K., Brummer, T., and Chen, P. R., 2011, "Space-Time Fluid-Structure Interaction Modeling of Patient-Specific Cerebral Aneurysms," Int. J. Numer. Methods Biomed. Eng., **27**(11), pp. 1665–1710.

[117] Mittal, S., and Tezduyar, T. E., 1995, "Parallel Finite Element Simulation of 3D Incompressible Flows-Fluid-Structure Interactions," Int. J. Numer. Methods Fluids, **21**(10), pp. 933–953.

[118] Neal, M. L., and Kerckhoffs, R., 2010, "Current Progress in Patient-Specific Modeling," Briefings Bioinf., **11**(1), pp. 111–126.

[119] Cebral, J. R., Castro, M. A., Burgess, J. E., Pergolizzi, R. S., Sheridan, M. J., and Putman, C. M., 2005, "Characterization of Cerebral Aneurysms for Assessing Risk of Rupture by Using Patient-Specific Computational Hemodynamics Models," Am. J. Neuroradiol., **26**(10), pp. 2550–2559.

[120] Karmonik, C., Klucznik, R., and Benndorf, G., 2008, "Comparison of Velocity Patterns in an AComA Aneurysm Measured With 2D Phase Contrast MRI and Simulated With CFD," Technol. Health Care, **16**(2), pp. 119–128.

[121] Ford, M. D., Nikolov, H. N., Milner, J. S., Lownie, S. P., DeMont, E. M., Kalata, W., Loth, F., Holdsworth, D. W., and Steinman, D. A., 2008, "PIV-Measured Versus CFD-Predicted Flow Dynamics in Anatomically Realistic Cerebral Aneurysm Models," ASME J. Biomech. Eng., **130**(2), p. 021015.

[122] Potočnik, B., Heric, D., Zazula, D., Cigale, B., and Bernad, D., 2005, "Construction of Patient Specific Virtual Models of Medical Phenomena," Informatica, **29**, pp. 209–218.

[123] Augsburger, L., Reymond, P., Fonck, E., Kulcsar, Z., Farhat, M., Ohta, M., Stergiopulos, N., and Rüfenacht, D. A., 2009, "Methodologies to Assess Blood Flow in Cerebral Aneurysms: Current State of Research and Perspectives," J. Neuroradiol., **36**(5), pp. 270–277.

[124] Hollnagel, D. I., Summers, P. E., Poulikakos, D., and Kollias, S. S., 2009, "Comparative Velocity Investigations in Cerebral Arteries and Aneurysms: 3D Phase-Contrast MR Angiography, Laser Doppler Velocimetry and Computational Fluid Dynamics," NMR Biomed., **22**(8), pp. 795–808.

[125] Jeong, W., and Rhee, K., 2012, "Hemodynamics of Cerebral Aneurysms: Computational Analyses of Aneurysm Progress and Treatment," Comput. Math. Methods Med., **2012**(4), pp. 1–11.

[126] Castro, M. A., Putman, C. M., and Cebral, J. R., 2006, "Patient-Specific Computational Modeling of Cerebral Aneurysms With Multiple Avenues of Flow From 3D Rotational Angiography Images," Acad. Radiol., **13**(7), pp. 811–821.

[127] Castro, M. A., Putman, C. M., and Cebral, J. R., 2006, "Computational Fluid Dynamics Modeling of Intracranial Aneurysms: Effects of Parent Artery Segmentation on Intra-Aneurysmal Hemodynamics," Am. J. Neuroradiol., **27**(8), pp. 1703–1709.

[128] Marzo, A., Singh, P., Reymond, P., Stergiopulos, N., Patel, U., and Hose, R., 2009, "Influence of Inlet Boundary Conditions on the Local Haemodynamics of Intracranial Aneurysms," Comput. Methods Biomech. Biomed. Eng., **12**(4), pp. 431–444.

[129] Marzo, A., Singh, P., Larrabide, I., Radaelli, A., Coley, S., Gwilliam, M., Wilkinson, I. D., Lawford, P., Reymond, P., Patel, U., Frangi, A., and Hose, D. R., 2011, "Computational Hemodynamics in Cerebral Aneurysms: The Effects of Modeled Versus Measured Boundary Conditions," Ann. Biomed. Eng., **39**(2), pp. 884–896.

[130] Shojima, M., Oshima, M., Takagi, K., Torii, R., Hayakawa, M., Katada, K., Morita, A., and Kirino, T., 2004, "Magnitude and Role of Wall Shear Stress on Cerebral Aneurysm: Computational Fluid Dynamic Study of 20 Middle Cerebral Artery Aneurysms," Stroke, **35**(11), pp. 2500–2505.

[131] Bazilevs, Y., Hsu, M.-C., Zhang, Y., Wang, W., Liang, X., Kvamsdal, T., Brekken, R., and Isaksen, J. G., 2010, "A Fully-Coupled Fluid-Structure Interaction Simulation of Cerebral Aneurysms," Comput. Mech., **46**(1), pp. 3–16.

[132] Raschi, M., Mut, F., Byrne, G., Putman, C. M., Tateshima, S., Viñuela, F., Tanoue, T., and Tanishita, K., 2012, "CFD and PIV Analysis of Hemodynamics in a Growing Intracranial Aneurysm," Int. J. Numer. Methods Biomed. Eng., **28**(2), pp. 214–228.

[133] Miura, Y., Ishida, F., Umeda, Y., Tanemura, H., Suzuki, H., Matsushima, S., Shimosaka, S., and Taki, W., 2013, "Low Wall Shear Stress is Independently Associated With the Rupture Status of Middle Cerebral Artery Aneurysms," Stroke, **44**, pp. 519–521.

[134] Omodaka, S., Sugiyama, S.-I., Inoue, T., Funamoto, K., Fujimura, M., Shimizu, H., Hayase, T., Takahashi, A., and Tominaga, T., 2012, "Local Hemodynamics at the Rupture Point of Cerebral Aneurysms Determined by Computational Fluid Dynamics Analysis," Cerebrovasc. Dis. (Basel, Switzerland), **34**(2), pp. 121–129.

[135] Fisher, C., and Rossmann, J. S., 2009, "Effect of Non-Newtonian Behavior on the Hemodynamics of Cerebral Aneurysm," ASME J. Biomech. Eng., **131**(9), p. 091004.

[136] Perktold, K., Peter, R., and Resch, M., 1989, "Pulsatile Non-Newtonian Blood Flow Simulation Through a Bifurcation With an Aneurysm," Biorheology, **26**, pp. 1011–1030.

[137] Valencia, A., Zarate, A., Galvez, M., and Badilla, L., 2006, "Non-Newtonian Blood Flow Dynamics in a Right Internal Carotid Artery With a Saccular Aneurysm," Int. J. Numer. Methods Fluids, **50**(6), pp. 751–764.

[138] Wang, S. Z., Chen, J. L., Ding, G. H., Lu, G., and Zhang, X. L., 2010, "Non-Newtonian Computational Hemodynamics in Two Patient-Specific

Cerebral Aneurysms With Daughter Saccules," J. Hydrodyn., **22**(5), pp. 639–646.

[139] Bernabeu, M. O., Nash, R. W., Groen, D., Carver, H. B., Hetherington, J., Krüger, T., and Coveney, P. T., 2013, "Impact of Blood Rheology on Wall Shear Stress in a Model of the Middle Cerebral Artery," Interface Focus, **3**(3), p. 20120094.

[140] Valencia, A., Guzmán, A. M., Finol, E. A., and Amon, C. H., 2006, "Blood Flow Dynamics in Saccular Aneurysm Models of the Basilar Artery," ASME J. Biomech. Eng., **128**(4), pp. 516–526.

[141] Evju, O., Valen-Sendstad, K., and Mardal, K. A., 2013, "A Study of Wall Shear Stress in 12 Aneurysms With Respect to Different Viscosity Models and Flow Conditions," J. Biomech., **46**(16), pp. 2802–2808.

[142] Dimakopoulos, Y., Syrakos, A., Georgios, G. C., Papadopoulos, K., and Tsamopoulos, J., 2014, "Effect of RBC Migration Phenomena on the Hemodynamics in Stenotic Microvessels Under Pulsating Flow Conditions," Book of Abstracts of the 9th Annual European Rheology Conference, Karlsruhe, Germany, Apr. 8–11, Vol. 75, p. 58.

[143] Steinman, D. A., Hoi, Y., Fahy, P., Morris, L., Walsh, M. T., Aristokleous, N., Anayiotos, A. S., Papaharilaou, Y., Arzani, A., Shadden, S. C., Berg, P., Janiga, G., Bols, J., Segers, P., Bressloff, N. W., Cibis, M., Gijsen, F. H., Cito, S., Pallarés, J., Browne, L. D., Costelloe, J. A., Lynch, A. G., Degroote, J., Vierendeels, J., Fu, W., Qiao, A., Hodis, S., Kallmes, D. F., Kalsi, H., Long, Q., Kheyfets, V. O., Finol, E. A., Kono, K., Malek, A. M., Lauric, A., Menon, P. G., Pekkan, K., Moghadam, M. E., Marsden, A. L., Oshima, M., Katagiri, K., Peiffer, V., Mohamied, Y., Sherwin, S. J., Schaller, J., Goubergrits, L., Usera, G., Mendina, M., Valen-Sendstad, K., Habets, D. F., Xiang, J., Meng, H., Yu, Y., Karniadakis, G. E., Shaffer, N., and Loth, F., 2013, "Variability of Computational Fluid Dynamics Solutions for Pressure and Flow in a Giant Aneurysm: The ASME 2012 Summer Bioengineering Conference CFD Challenge," ASME J. Biomech. Eng., **135**(2), p. 021016.

[144] Valen-Sendstad, K., and Steinman, D. A., 2014, "Mind the Gap: Impact of Computational Fluid Dynamics Solution Strategy on Prediction of Intracranial Aneurysm Hemodynamics and Rupture Status Indicators," Am. J. Neuroradiol., **35**(3), pp. 544–545.

[145] Janela, J., Moura, A., and Sequeira, A., 2010, "Towards a Geometrical Multiscale Approach to Non-Newtonian Blood Flow Simulations," *Advances in Mathematical Fluid Mechanics*, R. Rannacher, A. Sequeira (eds) Springer, Berlin, pp. 295–09.

[146] Forsyth, A. M., Wan, J., Owrutsky, P. D., Abkarian, M., and Stone, H. A., 2011, "Multiscale Approach to Link Red Blood Cell Dynamics, Shear Viscosity, and ATP Release," Proc. Natl. Acad. Sci. U.S.A, **108**, pp. 10986–10991.

[147] Xu, Z., Chen, N., Shadden, S. C., Marsden, J. E., Kamocka, M. M., Rosen, E. D., and Alber, M., 2009, "Study of Blood Flow Impact on Growth of Thrombi Using a Multiscale Model," Soft Matter, **5**, pp. 769–779.

[148] Grinberg, L., Fedosov, D. A., and Karniadakis, G. E., 2013, "Parallel Multiscale Simulations of a Brain Aneurysm," J. Comput. Phys., **244**, pp. 131–147.